J. Fluid Mech. (2003), *vol.* 482, *pp.* 51–90. © 2003 Cambridge University Press
DOI: 10.1017/S0022112003003926 Printed in the United Kingdom

On the disturbance growth in an asymptotic suction boundary layer

By J. H. M. FRANSSON AND P. H. ALFREDSSON

KTH Mechanics, S-100 44, Stockholm, Sweden

(Received 3 January 2002 and in revised form 2 December 2002)

An experimental and theoretical study on the effect of boundary layer suction on the laminar–turbulent transition process has been carried out. In the study an asymptotic suction boundary layer was established in a wind tunnel with a free-stream velocity of $5.0\,\mathrm{m\,s^{-1}}$. Wall-normal suction (suction velocity $1.44\,\mathrm{cm\,s^{-1}}$) was applied over a large area and the boundary layer was nearly constant over a length of 1800 mm. Measurements were made both with and without suction so comparisons between the two cases could easily be made. Measurements of the development of the mean velocity distribution showed good agreement with theory. The Reynolds number based on the displacement thickness for the suction boundary layer was 347. Experiments on both the development of forced Tollmien–Schlichting (TS) waves and boundary layer disturbances introduced by free-stream turbulence were carried out. Spatial linear stability calculations for TS-waves, where the wall-normal velocity component is accounted for, were carried out for comparison with the experiments. This comparison shows satisfactory agreement even though the stability of the asymptotic suction profile is somewhat overpredicted by the theory. Free-stream turbulence (FST) was generated by three different grids, giving turbulence intensities at the leading edge of the plate between 1.4% and 4.0%. The FST induces disturbances in the boundary layer and it was shown that for the present suction rate the disturbance level inside the boundary layer is constant and becomes proportional to the FST intensity. In all cases transition was prevented when suction was applied whereas without suction the two highest levels of grid turbulence gave rise to transition. Despite a twofold reduction in the boundary layer thickness in the suction case compared to the no suction case the spanwise scale of the streaky structures was almost constant.

1. Introduction

One area of significant recent interest in fluid dynamics is laminar flow control (LFC). A possible method of LFC is to apply suction at the wall. A description of this control method is given in Joslin (1998), where it is pointed out that LFC is a method to delay the laminar–turbulent transition and not to relaminarize the flow. The energy cost is typically one order of magnitude higher in the latter case, which makes the distinction appropriate since the optimal performance is not obtained (as one might believe) when the suction completely absorbs the boundary layer. The more suction that is used the steeper the velocity gradient of the boundary layer at the wall, implying an increase in skin friction. Therefore, the balance between maintaining laminar flow and keeping a low energy consumption is actually the optimal performance.

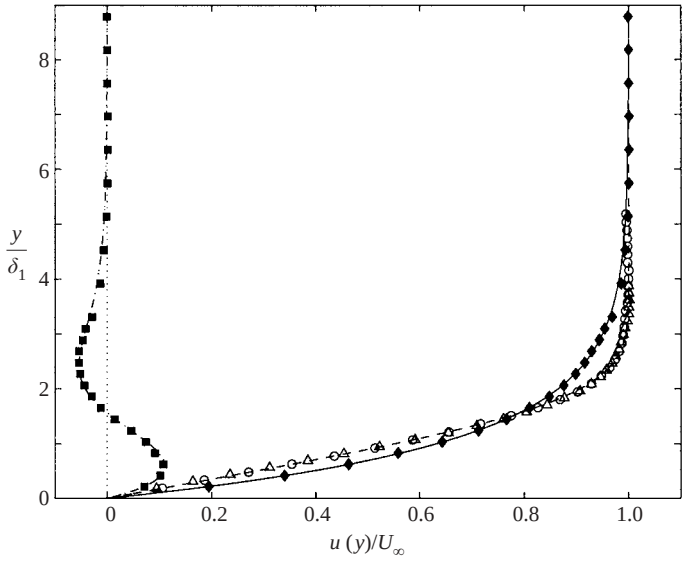

FIGURE 1. Velocity profiles for the Blasius and the asymptotic suction boundary layers. No suction (unfilled symbols), suction (filled symbols) and theory (lines). Asymptotic suction profile (solid line, ◆) at $x = 1800$, Blasius profiles (dashed line) at $x = 300$ mm (○) and at $x = 1800$ mm (△). –·–·, ■, The difference between the two velocity profiles.

The present paper describes theoretical and experimental work on laminar–turbulent transition in a flat-plate boundary layer when uniform suction through the surface is applied. (In a physical situation uniform suction is an idealization, since the pore size is finite. If the ratio between the boundary layer thickness and the pore size is large the suction will be close to uniform.) A special case is when the so-called asymptotic suction profile is obtained. This flow condition is obtained at some distance downstream the leading edge of a flat plate when uniform suction is applied over a large area. An interesting feature is that an analytic solution of the uniform suction problem may be derived from the boundary layer equations, resulting in an exponential profile (the asymptotic suction profile). The suction has a similar influence on the profile to that of favourable pressure gradient and makes the profile in the fully developed asymptotic region much more stable than the Blasius profile.

The asymptotic boundary layer flow has been dealt with extensively in text books, see for instance Schlichting (1979), and the theory for the mean flow is straightforward. One can easily show that the boundary layer profile $u(y)$ becomes

$$u/U_\infty = 1 - \mathrm{e}^{-yV_0/\nu}, \tag{1.1}$$

where U_∞, V_0 and ν are the constant free-stream velocity, the suction velocity and the kinematic viscosity, respectively (x, y and z denote the streamwise, wall-normal and spanwise coordinate directions). This expression was first derived by Griffith & Meredith (1936) according to both Jones & Watson (1963) and Schlichting (1979). In figure 1 experimental data with corresponding theoretical curves are plotted to show the comparison between the Blasius and the asymptotic suction profiles. The asymptotic boundary layer thickness can be shown to be directly proportional to ν/V_0 and the Reynolds number (Re) based on the boundary layer displacement thickness

(δ_1) becomes

$$Re = U_\infty / V_0 (= 1/C_q),$$

where C_q is the suction coefficient.

To obtain the stability characteristics of the suction boundary layer the normal velocity component of the mean flow, i.e. the suction velocity at the wall, can be incorporated into the disturbance equation and this gives a slightly modified Orr–Sommerfeld (OS) equation. Also, the boundary condition of the normal fluctuation velocity needs to be considered, but the standard boundary condition can be used in the limit when the permeability approaches zero. Hocking (1975) showed that the critical Reynolds number (Re_c), i.e. the lowest Reynolds number for which two-dimensional waves become amplified, increases by two orders of magnitude compared to the Blasius boundary layer. Fransson & Alfredsson (2003) showed that for the case of channel flow with permeable walls and cross-flow the situation becomes more complicated and can give rise to both stabilization and destabilization depending on the rate of cross-flow. The critical Reynolds number is lowered by an order of magnitude ($Re_c = 667.4$) compared to plane Poiseuille flow at a cross-flow velocity of 5.7% of the streamwise velocity.

1.1. *Laminar–turbulent transition scenarios*

1.1.1. *Tollmien–Schlichting-wave-dominated transition*

For low environmental disturbances the transition scenario from laminar to turbulent flow on a flat-plate boundary layer is quite well understood. This class of transition starts with instability waves that are generated in the receptivity process taking place close to the leading edge. The initial growth of these waves may be described by Fourier modes $\propto e^{i(\alpha x - \omega t)}$, where for spatially growing waves the wavenumber α is complex, $\alpha = \alpha_r + i\alpha_i$ and the angular frequency ω is real. For such a mode the linear disturbance equation gives rise to the well-known OS-equation. These waves grow/decay exponentially and the critical Reynolds number is, according to Squire's theorem, obtained for a two-dimensional wave. In figure 2 the stability diagram (based on linear parallel theory) is given for the Blasius profile. The solid lines are contours of the growth factor (α_i) and the bold solid line is the neutral stability curve, i.e. the contour line of $\alpha_i = 0$. The dash-dotted lines correspond to contour lines of constant wavenumber (α_r). The Reynolds number (Re) (which will be used throughout this paper) is based on the displacement thickness (δ_1), and F is the non-dimensionalized frequency defined as $F = (\omega\nu/U_\infty^2) \times 10^6$.

If a TS-wave in a Blasius boundary layer reaches high enough amplitude ($\gtrsim 1\%$ of U_∞), three-dimensional waves and vortices develop (still laminar) that give rise to the appearance of turbulent spots which merge and bring the whole flow into a fully turbulent state. The first successful wind tunnel experiment on TS-waves was carried out and reported by Schubauer & Skramstad (1948). However, these results were not in fully agreement with theory and for a long time the discrepancy between linear parallel stability theory and experiments was believed to be due to the non-parallel effect of a growing boundary layer. However, Fasel & Konzelmann (1990) found through direct numerical integration of the Navier–Stokes equations that this effect is quite small and that it hardly influences the amplitude and phase distributions. Later, parabolized stability calculations by Bertolotti (1991) showed that the non-parallel effect becomes significantly stronger for three-dimensional disturbances. Finally, the experiments by Klingmann *et al.* (1993), performed with a specially designed asymmetric leading edge (in order to eliminate the pressure suction peak), showed excellent agreement with

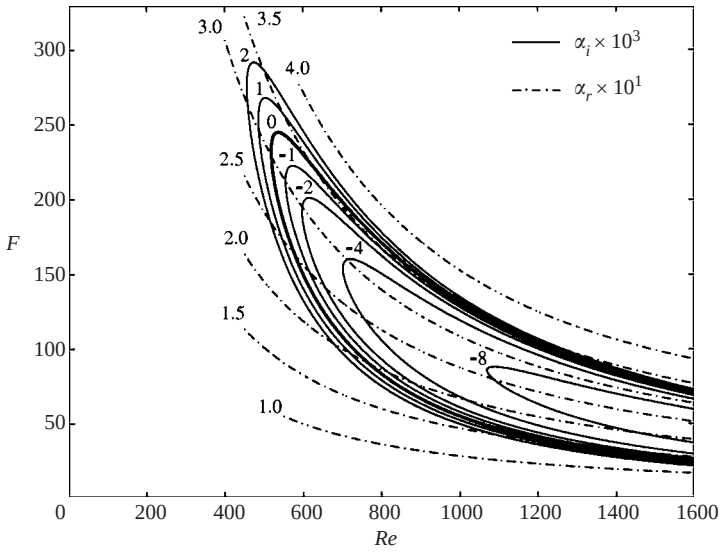

FIGURE 2. Spatial stability curves for two-dimensional waves in a Blasius boundary layer. Solid lines are for constant imaginary parts of the streamwise wavenumber (α_i) and dash-dotted for constant real parts (α_r). The bold solid line is the neutral stability curve. The displacement thickness (δ_1) is the characteristic length scale.

non-parallel theory, which is close to the parallel theory results for two-dimensional disturbances.

1.1.2. *By-pass transition and streaky structure*

It is well known that for the Blasius boundary layer free-stream turbulence (FST) induces disturbances into the boundary layer which give rise to streamwise-oriented structures of low- and high-speed fluid (see e.g. Kendall 1985; Westin 1997; Jacobs & Durbin 2001; Matsubara & Alfredsson 2001; Fransson & Westin 2001 for thorough investigations of such a flow). These structures grow in amplitude and establish a spanwise size which is of the order of the boundary layer thickness far away from the leading edge. When the streaks reach a certain amplitude they break down to turbulence, probably through a secondary instability mechanism (see e.g. Andersson *et al.* 2001). This type of boundary layer transition can be viewed as a case of by-pass transition (Morkovin 1969). It is a relatively rapid process by-passing the traditional TS-wave-dominated transition process, resulting in breakdown to turbulence at subcritical Reynolds numbers when compared with the value predicted by traditional theory. Nonlinear theories have been tested (see e.g. Orszag & Patera 1983) in order to find a theory that matched experimental results. However, the nonlinear terms of the Navier–Stokes equations can be shown not to be part of the growth mechanism (see Drazin & Reid 1981). A possible mechanism governing this type of transition scenario is the transient growth. An explanation of this mechanism is given in e.g. Schmid & Henningson (2001) and arises due to the non-orthogonality of the OS and Squire eigenmodes. Superposition of such decaying modes may first produce an algebraic growth followed by an exponential decay, denoted transient growth. The 'lift-up' mechanism proposed by Landahl (1980) is the cornerstone of the algebraic growth in the study of transient growth. Small perturbations in the wall-normal direction induce large disturbances in the streamwise direction due to

the lift-up of low-speed fluid that originally maintains its horizontal momentum. The presence of viscosity will eventually damp the growth and finally make the disturbance decay. Some recent publications on the by-pass transition and the transient growth mechanism are Luchini (2000), Reshotko (2001), and Andersson *et al.* (2001).

1.2. *Previous work on suction*

Some experimental work on the asymptotic suction boundary layer has already been done, but mainly devoted to determination of the mean flow (see Schlichting 1979 and references therein). TS-wave as well as FST experiments in a fully asymptotic suction boundary layer, which will be presented in this paper, have not previously been carried out. However, in connection with drag reduction with experiments (i.e. LFC) suction through spanwise slots, porous panels and discrete holes has been applied (see e.g. Pfenninger & Groth 1961; Reynolds & Saric 1986; and MacManus & Eaton 2000 as well as Roberts *et al.* 2001, respectively). A general review of various types of surfaces and of the results achieved in wind tunnel tests is given by Gregory (1961), where practical applications on aircraft are discussed. The flow characteristics through laser-drilled titanium sheets were investigated by Poll, Danks & Humphreys (1992*b*) and were shown to be laminar, incompressible and pipe like. Poll, Danks & Davies (1992*a*) conducted an experiment on a cylinder made of a similar laser-drilled titanium sheet. Suction was found to have a powerful effect upon cross-flow-induced transition.

In an experimental and numerical study performed by MacManus & Eaton (2000) the flow physics of boundary layer suction through discrete holes was investigated. The aim was to use a realizable design and find a critical suction criterion for transonic cruise conditions. They showed that the suction may destabilize the flow by introduction of contra-rotating streamwise vortices but that for small enough perforations ($d/\delta_1 < 0.6$) transition is not provoked by suction, independent of suction velocity.

Roberts *et al.* (2001) found that two types of instability are possible when non-uniformities of suction are present. The first one is connected to the classical TS-wave that is modified due to the non-uniformities and the second concerns streamwise vortices that are induced due to the non-uniformities alone. The latter instability was triggered by a finite band of suction wavenumbers and the strength of this instability was shown to increase almost linearly with the amplitude of the suction non-uniformities and flow Reynolds number.

Applying continuously distributed suction over a large area may not be the optimal way of performing active control practically, since the energy consumption becomes relatively high. Another approach would be to use selective suction to control the growth of unstable fluctuations. This type of control must be on a detectable quantity, such as e.g. low-speed streaks. The appearance of streaks with alternate low- and high-speed velocity observed in a laminar boundary layer subjected to high levels of free-stream turbulence is also found in the near-wall region of a turbulent boundary layer. Together with the intermittent bursts or turbulence production events these are usually referred to as coherent structures. Controlled experiments have been performed, see e.g. Myose & Blackwelder (1995) and Lundell (2000), in order to reduce the instability and delay the breakdown of the low-speed streaks in laminar flows. Myose & Blackwelder (1995) achieved successful control of the breakdown of Görtler vortices, by pointwise suction of low-speed momentum from the low-speed streak and in that manner delayed the transition by producing a fuller profile in the normal direction and by eliminating the difference between low- and high-speed

regions in the spanwise direction. A similar technique was used by Lundell (2000) who generated streaks in a plane channel flow by applying suction through streamwise slots. Secondary instabilities were forced randomly by speakers and were successfully controlled by localized suction some distance downstream.

1.3. *Layout of the paper*

In § 2 the boundary layer equations for the evolution of the asymptotic suction boundary layer are put forward as well as the stability equations when the normal velocity is taken into account. Some results on both the mean profile evolution and stability are then given for the asymptotic suction boundary layer. The design philosophy of the leading edge of the experimental plate is described in § 3 together with characterization of the porous material, the detailed construction of the flat plate, and the TS-wave excitation method. The different turbulent length scales and energy spectra generated by the three different turbulence-generating grids are also given. In § 4 the experimental results are given for the Blasius flow above the porous plate and the streamwise baseline flow of the suction case, as well as the corresponding TS-waves results. Furthermore, results of the disturbance evolution in both the no suction and suction cases when FST is present are given and compared in detail. It is clearly shown that suction can change the disturbance growth rate dramatically and that transition to turbulence can be prevented.

2. Boundary layer evolution and stability concepts

2.1. *Evolution region*

When uniform wall-normal surface suction is applied over a large area the well-known asymptotic suction profile will be reached after some evolution region. If there is an impermeable area from the leading edge to where the suction starts the boundary layer will be allowed to grow and a Blasius velocity profile will be developed for a zero-pressure-gradient flow. In the evolution region the profile will then undergo a transformation from the Blasius state to the asymptotic suction state. This spatial evolution can with a simple approach be described through a non-dimensional evolution equation. The first step is to introduce a stream function according to

$$\psi = \sqrt{\nu x U_\infty} f(\xi, \eta),$$

$$\xi = x \frac{V_0}{U_\infty} \sqrt{\frac{U_\infty}{\nu x}}, \qquad \eta = y \sqrt{\frac{U_\infty}{\nu x}}.$$

The streamwise and normal velocity components are recovered through

$$u(\eta) = U_\infty \frac{\partial f}{\partial \eta}, \qquad v(\eta) = \sqrt{\frac{U_\infty \nu}{4x}} \left(\eta \frac{\partial f}{\partial \eta} - \xi \frac{\partial f}{\partial \xi} - f \right),$$

respectively. Applying this to the boundary layer equations we obtain the following third-order nonlinear partial differential equation:

$$\frac{\partial^3 f}{\partial \eta^3} + \frac{1}{2} f \frac{\partial^2 f}{\partial \eta^2} + \frac{1}{2} \xi \left(\frac{\partial f}{\partial \xi} \frac{\partial^2 f}{\partial \eta^2} - \frac{\partial f}{\partial \eta} \frac{\partial^2 f}{\partial \eta \partial \xi} \right) = 0, \tag{2.1}$$

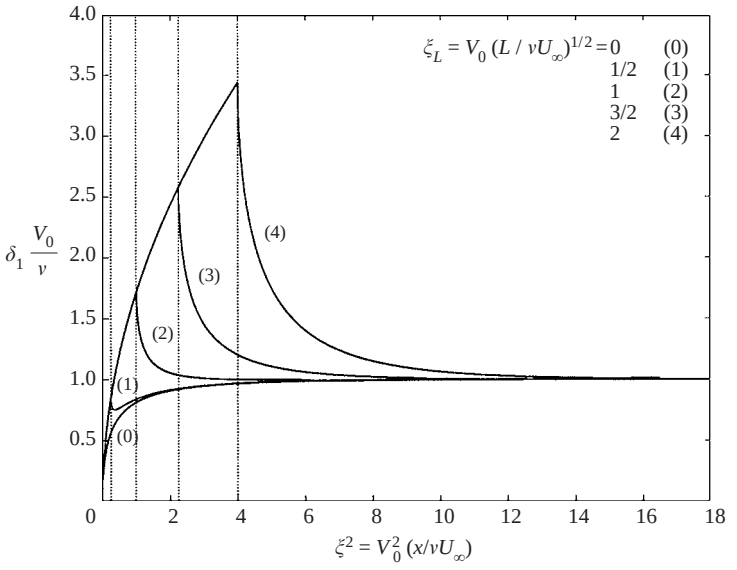

FIGURE 3. The displacement thickness evolution from the evolution equation (2.1) vs. the downstream distance to the power of two. See text for comments.

with the corresponding boundary conditions

$$\left.\begin{array}{ll} f = \xi & \text{(suction)} \\ \dfrac{\partial f}{\partial \eta} = 0 & \text{(no-slip)} \end{array}\right\} \quad \text{at} \quad \eta = 0 \quad \text{and} \quad \frac{\partial f}{\partial \eta} \to 1 \quad \text{as} \quad \eta \to \infty.$$

Over the impermeable entry length a Blasius boundary layer is assumed to develop and is given as input to the evolution equation. The boundary conditions at permeable surfaces are not obvious. Taylor (1971) discussed the boundary conditions and concluded that due to the open structure of a porous solid with large pores the external surface stress may produce a tangential flow below the surface resulting in the no-slip condition for the mean flow not being valid. This surface velocity is assumed to depend on the mean tangential stress in the fluid outside the porous material, the permeability and another material (porous) connected parameter. This model showed that experimental results agreed well with calculation but only for large permeabilities.

The first solution from such an evolution equation with an impermeable entry length was obtained by Rheinboldt (1956) through a series expansion. The ansatz of a stream function and non-dimensionalized variables for deriving the evolution equation are not to be confused with similarity solutions. The stream function is dependent on two variables and becomes 'similar' when the asymptotic suction state is reached. In figure 3 the displacement thickness (δ_1) of the profiles in the evolution region is plotted. The different curves can be seen for different impermeable entry lengths shown with the dotted lines, i.e. they are for different values of the initial length (ξ_L). These are the positions where suction starts and all the curves have in common that after some evolution region they all merge together to a value of unity which corresponds to the asymptotic suction region. Recall that the asymptotic suction profile possesses an analytic expression which implies that all the characteristic length scales are exact, e.g.

$\delta_1 = \nu/V_0$, $\delta_2 = (1/2)\delta_1$ and $\delta_{0.99} = \delta_1 \log(100)$, where δ_2 and $\delta_{0.99}$ are the momentum thickness and the actual boundary layer thickness respectively.

2.2. *Modal stability characteristics*

When deriving the Orr–Sommerfeld (OS) and Squire equations the so-called parallel flow assumption is made, which means that changes in x of the mean flow are neglected. For the continuous suction case where the mean wall-normal velocity component (V_0) is uniform and constant this assumption is exact, although the flow is not parallel to the wall. In order to neglect the V-component the suction rate has to be small. However, the parallel flow assumption is not needed since the cross-flow term can be considered easily.

When the baseline flow, $\overline{U} = (U(y), V_0, 0)$, is introduced into the linearized stability equations one extra term is added to each equation, namely $V_0 \partial u/\partial y$, $V_0 \partial v/\partial y$, and $V_0 \partial w/\partial y$. Here (u, v, w) denotes the fluctuation velocity components in the (x, y, z) directions, respectively. The expression for the pressure, obtained by taking the divergence of the linearized momentum equations, does not change (compared to the no suction case) since the additional terms fulfil the continuity equation and therefore cancel out. After the pressure expression is used in the v-equation of momentum we apply the normal-mode hypothesis. Using the standard notation for the spatial theory, α represents the complex streamwise wavenumber, ω the real angular frequency and β the real spanwise wavenumber which is used in order to possibly include oblique modes. The modified OS-equation can then be written as

$$\left[\left(-\mathrm{i}\omega + \mathrm{i}\alpha U - \frac{1}{Re}\mathscr{D}\right)(\mathscr{D}^2 - k^2) - \mathrm{i}\alpha U'' - \frac{1}{Re}(\mathscr{D}^2 - k^2)^2\right]\hat{v} = 0,$$

where $\mathscr{D} = \partial/\partial y$, $k^2 = \alpha^2 + \beta^2$ and $\hat{v}$ denotes the amplitude function of the eigenmode. This modified version of the OS-equation can be found in e.g. Drazin & Reid (1981). A modified Squire equation can equally be derived resulting in

$$\left[\left(-\mathrm{i}\omega + \mathrm{i}\alpha U - \frac{1}{Re}\mathscr{D}\right) - \frac{1}{Re}(\mathscr{D}^2 - k^2)\right]\hat{\Omega} = -\mathrm{i}\beta U'\hat{v},$$

where Ω is the normal vorticity. So far no change in the boundary conditions of the disturbance quantities has been made and indeed should not be necessary as long as the permeability of the porous material has a reasonably low value.

In the present study the homogeneous boundary condition was used, i.e. $\hat{v} = \mathscr{D}\hat{v} = \hat{\Omega} = 0$, in all calculations since the permeability of the chosen material can be considered small. Another boundary condition for the perturbations for a porous plate was suggested by Gustavsson (2000), where a pressure perturbation above the plate is added to Darcy's law. The result is an extra term for the boundary condition at the wall, which for small permeability would be negligible. This condition has so far not been verified experimentally.

Squire's theorem can be derived from the modified OS- and Squire equations in the usual way by identification of terms in the two-dimensional and three-dimensional cases. However, the extra terms do not contribute any additional condition to Squire's theorem.

2.3. *Numerical methods*

The evolution equation was solved with a spectral approach, with Chebyshev expansion in the wall-normal direction and a backward finite difference method in the

marching direction with a step size of $\mathrm{d}\xi = 0.001$. A built-in nonlinear equation solver in the commercially available software Matlab was used.

The stability calculations carried out on the Blasius and the asymptotic suction boundary layers in the present section are for the spatial spectrum, i.e. the set of equations are solved for α given a real frequency ω. The numerical method used for these calculations was also a spectral method with Chebyshev expansion of the dependent variable. The solution is then represented by a truncated sum of Chebyshev polynomials according to

$$\hat{v}(\tilde{y}) = \sum_{n=0}^{N} a_n \mathbb{T}_n^j(\tilde{y}) \quad \text{for} \quad \tilde{y} \in [-1, 1],$$

where N is the truncated value, a_n is the coefficient of the nth Chebyshev polynomial and the superscript j denotes the jth derivative of the Chebyshev polynomials. A domain mapping from the finite Chebyshev domain ($[-1, 1]$) into the semi-infinite physical domain of the boundary layer was made through $y = \frac{1}{2} y_\infty (1 - \tilde{y})$.

A spatial approach gives rise to a nonlinear eigenvalue problem where the eigenvalue appears as a fourth power in the normal velocity. This can be reduced to an eigenvalue equation of second power by a transformation of the independent variable according to Haj-Hariri (1988):

$$\begin{pmatrix} \hat{v} \\ \hat{\Omega} \end{pmatrix} = \begin{pmatrix} \hat{V} \\ \hat{E} \end{pmatrix} \mathrm{e}^{-\alpha y}. \tag{2.2}$$

In order to remove the nonlinearity in the eigenvalue problem, i.e. the remaining second-order α-terms of the $\hat{V}$-component, one can introduce a vector quantity according to

$$\boldsymbol{d} = \begin{pmatrix} \alpha \hat{V} \\ \hat{V} \\ \hat{E} \end{pmatrix},$$

which takes care of the nonlinear α-terms, see e.g. Schmid & Henningson (2001). After applying the transformation of equation (2.2) to the perturbation equations we obtain a linear eigenvalue problem which in matrix form can be written

$$\mathscr{L}\boldsymbol{d} = \alpha \mathscr{M}\boldsymbol{d}, \tag{2.3}$$

where

$$\mathscr{L} = \begin{pmatrix} -R_1 & -R_0 & 0 \\ I & 0 & 0 \\ 0 & -S & -T_0 \end{pmatrix} \quad \text{and} \quad \mathscr{M} = \begin{pmatrix} R_2 & 0 & 0 \\ 0 & I & 0 \\ 0 & 0 & T_1 \end{pmatrix}. \tag{2.4}$$

The R_i, T_i and S elements represent a number of terms and the only difference between the OS- and Squire equations and the modified OS- and Squire equations is the appearance of some extra terms marked with a brace underneath:

$$R_2 = 4\mathbb{T}^2 + 2\mathrm{i}URe\mathbb{T}^1 + \underbrace{2\mathbb{T}^1},$$

$$R_1 = -4\mathbb{T}^3 - \mathrm{i}URe\mathbb{T}^2 - \underbrace{3\mathbb{T}^2} - 2\mathrm{i}\omega Re\mathbb{T}^1 + 4\beta^2\mathbb{T}^1 + \mathrm{i}URe\beta^2\mathbb{T}^0 + \mathrm{i}U''Re\mathbb{T}^0 + \underbrace{\beta^2\mathbb{T}^0},$$

$$R_0 = \mathbb{T}^4 + \underbrace{\mathbb{T}^3} + \mathrm{i}\omega Re\mathbb{T}^2 - 2\beta^2\mathbb{T}^2 - \underbrace{\beta^2\mathbb{T}^1} - \mathrm{i}\omega\beta^2 Re\mathbb{T}^0 + \beta^4\mathbb{T}^0,$$

$$T_1 = \mathbb{T}^1 + \mathrm{i}URe\mathbb{T}^0 + \underbrace{\mathbb{T}^0},$$

$$T_0 = -\mathbb{T}^2 - \underbrace{\mathbb{T}^1} - \mathrm{i}\omega Re\mathbb{T}^0 + \beta^2\mathbb{T}^0,$$

$$S = \mathrm{i}\beta U' Re\mathbb{T}^0.$$

	Drazin & Reid		Schmid & Henningson	Present	
Case	Blasius	Asymp.	Blasius	Blasius	Asymp.
Re_c	520	54370	519.4	518.7	54382
α_c	0.3012	0.1555	0.303	0.3036	0.1555
c_r^c	0.3961	0.150	0.3965	0.3966	0.1499
F	229.3	0.429	231.3	232.1	0.429

TABLE 1. Critical values for the Blasius and the asymptotic suction boundary layer.

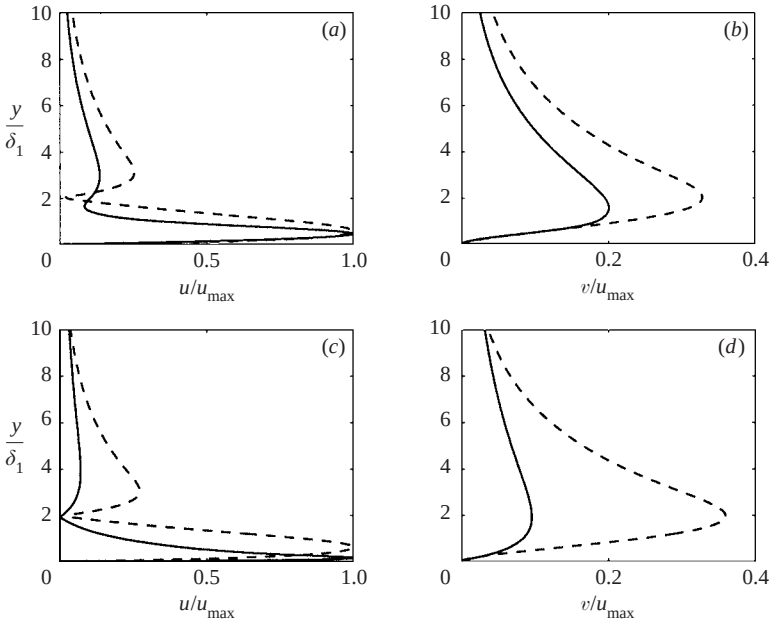

FIGURE 4. Eigenfunctions of both the Blasius (dashed lines) and the asymptotic suction case (solid lines) at $[Re, F] = [800, 125]$ in (a) and (b), and at their critical values (see table 1) in (c) and (d) respectively.

The notation for the elements in the matrixes (2.4) is chosen to be the same as used by Schmid & Henningson (2001).

The system of equations (2.3) was solved using a built-in eigenvalue problem solver in the mathematical software Matlab. A (temporal) program using search routines was developed in order to provide high accuracy of the critical values given in table 1. For a given wavenumber (α) this program searches for the Reynolds number at which the imaginary part of the phase velocity (c_i) is zero with an accuracy specified by the user and stops only for positive values of c_i. From there it chooses a new α by means of minimizing Re. The accuracy of α is also set by the user. The critical values in table 1 are in good agreement with other published values, see e.g. Drazin & Reid (1981) and Schmid & Henningson (2001), and the slightly varying values may be due to the solution method. Adding the V-component to the linearized stability equations, resulting in the modified OS-equation, has only a minor effect on the stability characteristics of the particular flow. The large stabilizing effect arises from the change in mean velocity profile, see e.g. Fransson (2001).

In figure 4 the difference between the Blasius and the asymptotic suction boundary layer eigenfunctions (streamwise and wall-normal) is illustrated for two different

parameter values. It is noteworthy that the maximum of the u-disturbance is found closer to the wall and that the ratio between the v- and the u-component is smaller for the asymptotic suction boundary layer than the Blasius boundary layer.

3. Experimental design and set-up

This section deals with the design of the experimental set-up, its construction, and the experimental techniques. In order to perform experiments in an asymptotic suction boundary layer a plate had to be designed and built with a suitable permeable surface material. This material was investigated in order to obtain appropriate characteristic properties. A new asymmetric leading edge was built and investigated.

3.1. *Experimental set-up*

The experiments were carried out in the MTL-wind tunnel at KTH. The test section is 7 m long, 0.8 m high and 1.2 m wide. The maximum free-stream velocity in the test section is more than $60\,\mathrm{m\,s^{-1}}$; however in the present study it is only used at low velocities. At these low velocities the turbulence intensity is around 0.02%–0.03%. The tunnel has good temperature stability characteristics due to a built-in heat exchanger and temperature control system. The wind tunnel is equipped with a computer-controlled 5 degrees of freedom traversing mechanism, which is convenient for boundary layer traverses as well as X-probe calibration. For a recent report on the tunnel characteristics see Lindgren & Johansson (2002).

A schematic of the experimental set-up is shown in figure 5, with the FST experimental set-up (*a*) and the TS-wave experimental set-up in (*b*). All the parts shown in (*a*) are also present in (*b*), except for the turbulence generating grids. A fine-meshed screen (mosquito type) was installed at the end of the test section just upstream of the trailing-edge flap (going into the diffuser). This created a pressure drop to compensate for the extra blockage below the plate due to suction channels and tubing (the total blockage in the tunnel is about 7%). In the present experiments the wind tunnel ceiling was adjusted so that the pressure gradient along the test section was close to zero for the no suction (Blasius flow) case. When suction was applied less than 1% of the flow in the test section was removed. This gives rise to a slight adverse pressure gradient; however the effect on the boundary layer flow is very small compared to the suction itself. The suction is achieved by a centrifugal fan positioned outside the test section and connected through a pressure vessel to the suction channels underneath the plate with vacuum cleaner tubing.

FST was generated by three different grids (two passive, B and E, and one active, G) mounted at different distances (x_{grid}) from the leading edge. The grids gave turbulence intensities ($Tu = u_{\mathrm{rms}}/U_\infty$) at the leading edge of the plate of 1.4%, 4.0% and 2.2%, respectively. In figures 6 and 7 the energy spectra (at $x = 400$ mm) and the FST decay in the free stream for the three different grids are plotted respectively. The typical power-law decay, $Tu = C(x - x_0)^b$, is applied to the Tu-decay data and plotted with solid lines in figure 7 for the three different grids. Here $x = 0$ is at the leading edge of the plate, whereas x_0 is a virtual origin. The constant C and exponent b are parameters to be determined through curve fitting to experimental data. In the curve fits b was set to -0.5 which is the value for fully isotropic turbulence. The virtual origin was determined consistently by taking the intersection point with the x/M-axis from plots of $1/Tu^2 = x/M$ (M being the mesh width of the grid). The fits are to the unfilled symbols in figure 7, which correspond to data collected when no suction was applied, whilst the filled symbols are when suction was applied.

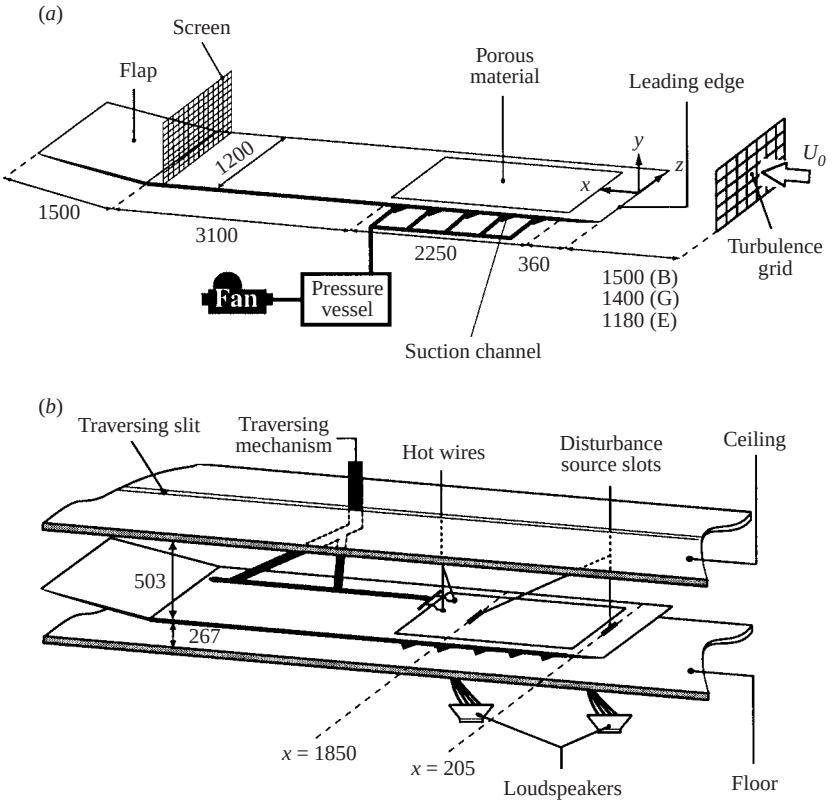

FIGURE 5. Schematic of the experimental set-up. (*a*) The three turbulence-generating grids give different turbulence intensities at the leading edge: $Tu_B = 1.4\%$, $Tu_E = 4.0\%$ and active grid G gave $Tu_G = 2.2\%$. (*b*) Two-dimensional waves are generated through two different slots in the plate. Dimensions in mm.

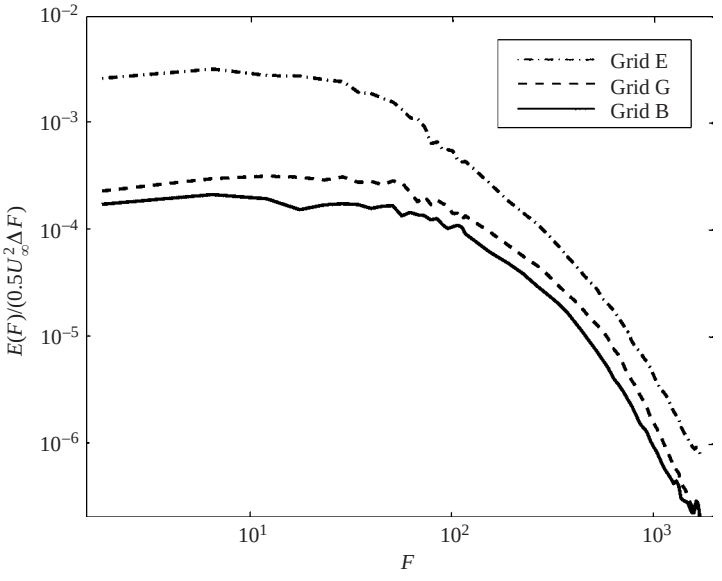

FIGURE 6. Energy spectra in the free stream from the three different grids at $x = 400$ mm.

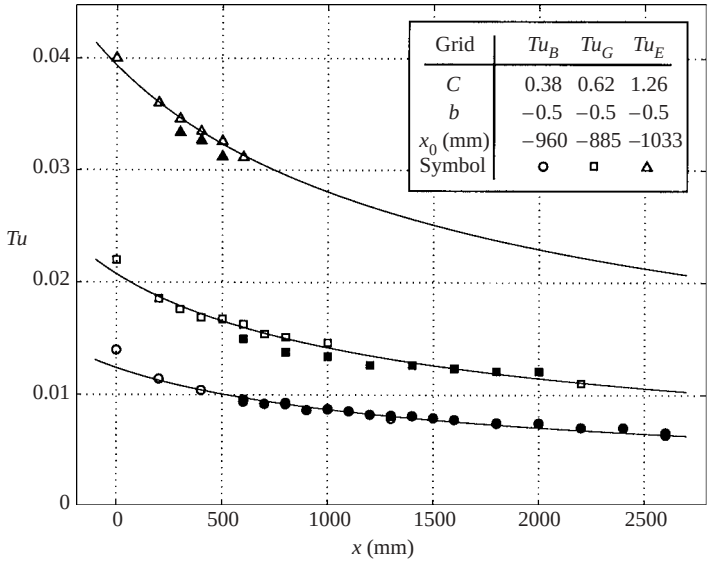

FIGURE 7. Turbulence decay in the free stream for the three different grids.

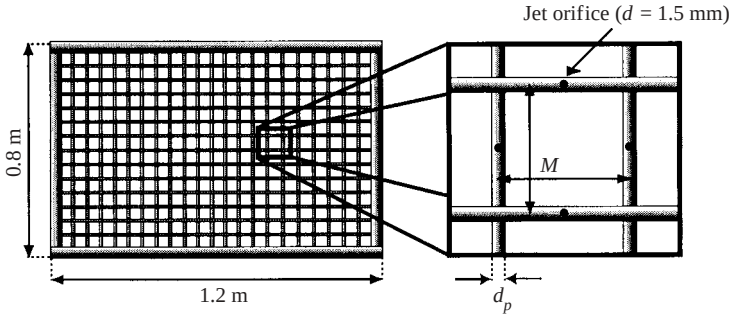

FIGURE 8. Active grid with main measures. $M = 50\,\text{mm}$ and $d_p = 5\,\text{mm}$ corresponding to a geometrical solidity (S_g) of 0.19. The total number of jet orifices is 254 and these are concentrated to the middle section of the grid.

The virtual origin is found to be displaced downstream of the grid for all cases (see figure 5*a*).

The active turbulence-generating grid, injecting secondary fluid upstream and in that way providing different *Tu*-levels, is described thoroughly in Fransson (2001), and in figure 8 a sketch of the grid is shown. The secondary fluid was driven by a modified vacuum cleaner. In the present investigation only one injection rate was applied. In figure 9 the evolution of both the longitudinal Taylor microscale (γ) and the integral lengthscale (Γ) are shown for the active grid. As expected the scales grow with downstream distance due to the dissipation of the smallest scales. The flow behind the active grid is homogeneous and isotropic $20M$ downstream of the grid position, which was checked with X-probe measurements. The two passive grids have been used extensively in previous works and the Taylor microscale data were obtained from Westin (1997). In table 2 the characteristic data of the turbulence-generating grids are summarized.

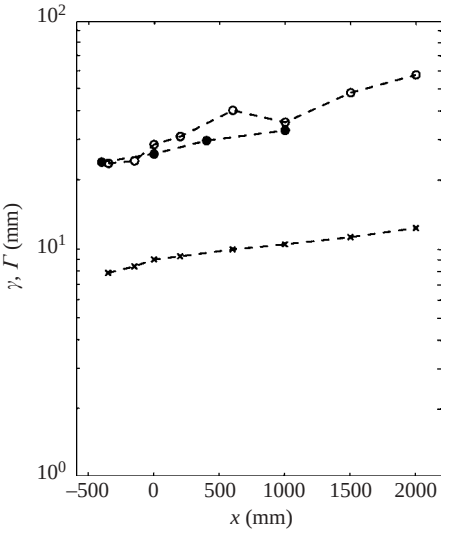

FIGURE 9. The Taylor (γ) and the integral (Γ) lengthscale evolution of the active grid (with injection) are plotted with ○ and × symbols respectively. Filled symbols of Γ are from spatial correlation measurements and unfilled from the autocorrelation. γ was determined from the autocorrelation alone, which gives a better estimate of this scale (see Fransson 2001 for further details).

Grid	Tu (%)	γ (mm)	M (mm)	d_p (mm)	S_g	Bar geometry	x_{grid} (mm)
B	1.4	7 ± 1	23	3.5	0.28	Round	-1500 ($65M$)
E	4.0	7 ± 1	50	10	0.36	Square	-1180 ($23.5M$)
G	2.2	9 ± 1	50	5	0.19	Round	-1400 ($28M$)

TABLE 2. Characteristic data of the turbulence-generating grids. For definitions of M, d_p and S_g see figure 8.

TS-waves were generated by alternating suction and blowing at the wall through a slot in a plug mounted in the plate. The slot is 330 mm long in the spanwise direction and 0.8 mm wide. Two plugs (slots) are present, one at $x = 205$ mm from the leading edge and one at $x = 1850$ mm. The latter is used for investigations in the fully developed asymptotic suction boundary layer. At this plug the porous plate was made impermeable over the whole spanwise width by sticking tape underneath the plate of width 50 mm in the flow direction where the plug was located (in order to maintain the two-dimensionality of the flow). The disturbance signal was generated by the computer through a D/A-board to an audio amplifier driving the loudspeakers. The loudspeakers are connected to the disturbance source through ten flexible tubes. A more thorough description of the disturbance generating system can be found in Elofsson (1998).

An asymmetric leading edge was specially designed for this experimental set-up, to give a relatively short pressure gradient region without a suction peak at the leading edge. The local pressure distribution near the leading edge influences the stability of the flow further downstream and therefore the design of the leading edge is an

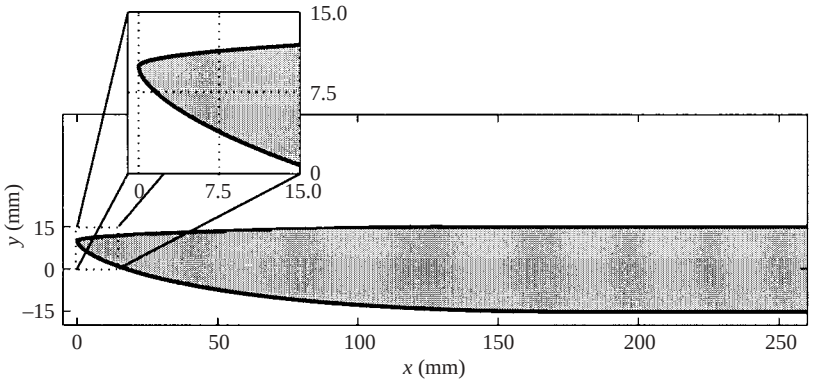

FIGURE 10. Final shape of the leading edge. The profile is described by two cubic Bézier curves.

important issue, see e.g. Klingmann *et al.* (1993). In figure 10 the final shape of the present leading edge, which is described by two cubic Bézier-curves, is shown. The commercial flow solver CFX 4.2 was used to design the leading edge for the present set-up. Two-dimensional laminar flow calculations were performed in the test section of the wind tunnel, i.e. the ceiling (upper wall) and the floor (lower wall) of the tunnel were simulated together with the plate. The present leading edge (with a thickness of 30 mm) gives a near-Blasius profile as close as 100 mm from the leading edge, when the suction channel and the suction tubing are absent. The analytic expression for the shape and further information about the design process together with experimental verification of the design can be found in Fransson (2001).

3.2. *Porous material*

For the permeable plate a porous plastic material was chosen. Compared to laser-drilled plates (discrete holes) it is only one tenth of the price and it has several advantages. For instance, the plastic material allows quite accurate hot-wire readings close to the wall due to the low heat conductivity, and its pore size and pore spacing is small, making the surface-normal velocity 'uniform' over the surface area, which is preferable in this experiment to that obtained with a plate with discrete holes.

The porous plates consist of a sintered plastic material with an average pore size of 16 μm (given by the manufacturer). One of the surfaces can be considered smooth and the other rough (the smooth one was used as the upper surface). The standard deviation of the roughness is about 0.38 μm on the smooth side, which was calculated from the surface roughness measurement in figure 11(a,b) (note the scale). In figure 11(c) the needle traces from the blown-up area in (a) is shown.

The flow properties of the porous material were characterized by a piston experiment in which the permeability of the porous material was determined by placing a piece of the porous material (thickness $t = 3.2$ mm) over the end of a 0.9 m, 4 cm diameter Plexiglas pipe and measuring the pressure drop over the porous material when a piston was forced through the pipe with a linear motor. This was performed at various velocities (V) in the range 0.4–1.2 cm s^{-1} and it was found that the pressure drop Δp varied in linear proportion to the flow velocity through the material (see figure 12). From this the permeability (k) of the material was determined from Darcy's law as $k = Vt\mu/\Delta p$, where μ is the dynamic viscosity, and was found to be $k = 3.7 \times 10^{-12}$ m^2.

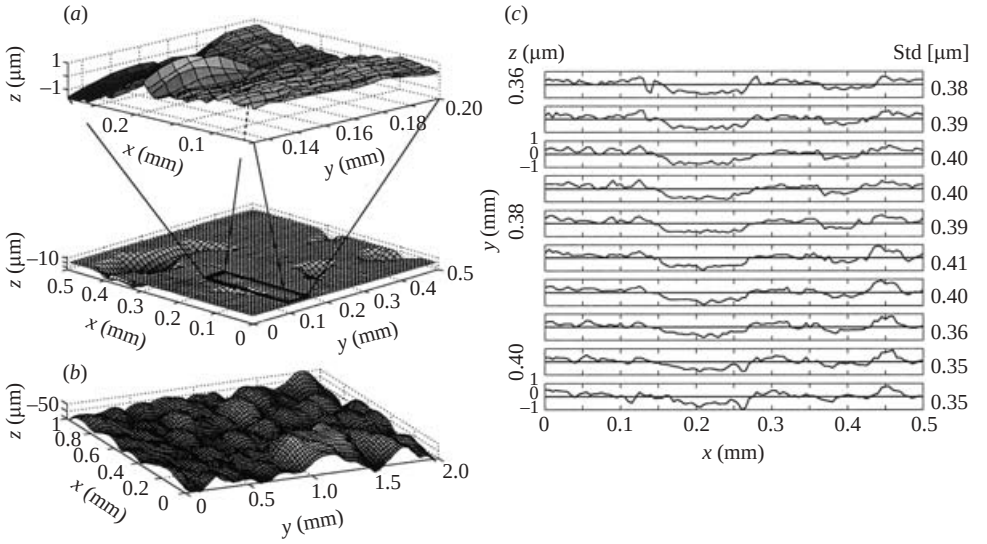

FIGURE 11. Surface roughness measurement of the porous material: (*a*) smooth side with a blown-up area and (*b*) rough side; (*c*) the surface traces from part of the area shown in (*a*).

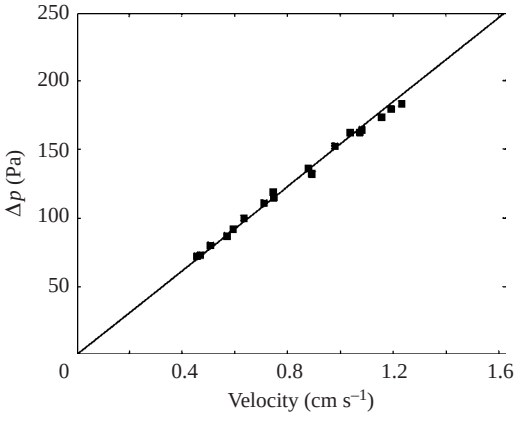

FIGURE 12. Piston-experiment result used to determine the permeability of the porous material.

A load-test of the porous material was performed in order to design the inner structure of the plate such that the surface deformation was sufficiently small when suction was applied. Three tests were performed and the average modulus of elasticity was determined to be 974 MPa. On the suction side longitudinal T-profiles a certain spanwise distance apart supported the plate. The spanwise distance (L_s) between these T-profiles was determined by assuming a 1.5 kPa pressure difference across the plate with the restriction of a bending deviation (w_b) of less than 1% of the boundary layer thickness (which was 5 mm resulting in $w_b = 50\,\mu$m). This gave $L_s = 58$ mm and the L_s finally used was 50 mm. Since the actual pressure difference that was applied in the final experiment was about 200–250 Pa there was a large margin in the load assumption.

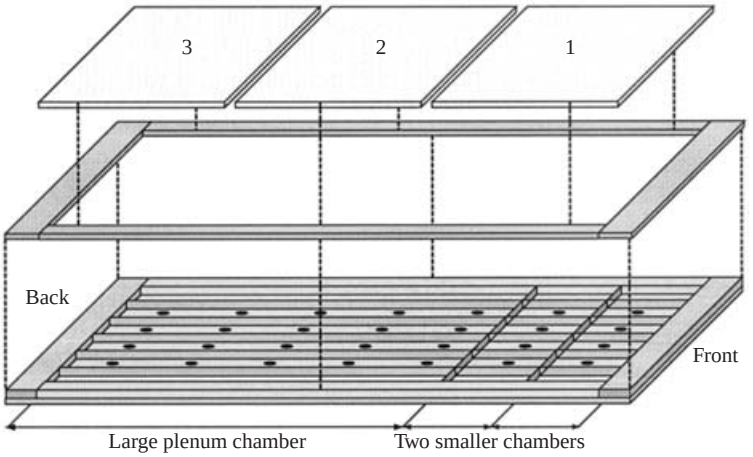

FIGURE 13. Schematic view of the plate construction. See text for comments.

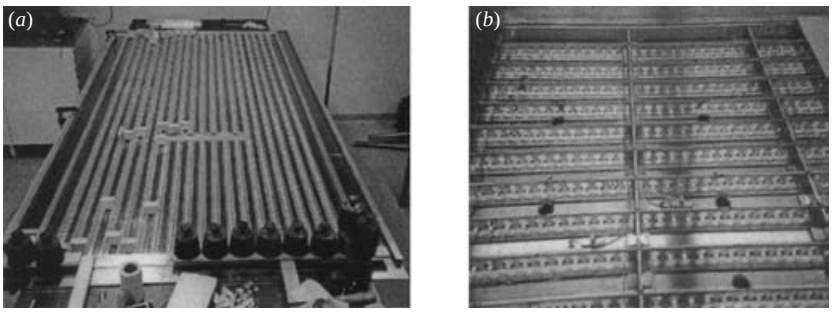

FIGURE 14. Photos of the construction work. (*b*) The two front plenum chambers together with the larger spanwise drilled suction holes and the pressure tubing for the static pressure measurements.

3.3. *Plate construction*

The test plate is built as a sandwich construction and a schematic is shown in figure 13. At the front of the plate the removable leading edge is mounted and at the back there is the possibility to extend the plate by additional plates of aluminium. The plate is constructed on a base plate of aluminium with a frame, and is designed with two 250 mm long plenum chambers starting 360 mm from the leading edge followed by a 1750 mm long plenum chamber. The subdivision into three chambers is for future work in which the suction rate is allowed to change with the downstream distance.

As mentioned above, inside the plenum chamber spacing elements made of hollowed T-profiles are glued, with a spanwise separation of 50 mm, in order to support the porous plates and avoid bending of the plates when suction is applied. On these T-profiles three porous plates with the total dimension $2250 \times 1000 \times 3.2\,\mathrm{mm}^3$ (length, width, thickness) were mounted in the frame plate. On a spanwise line in the base plate five large holes (30 mm) were drilled at nine positions to which nine suction channels were connected. This ensured a uniform pressure in the plenum chamber, which was checked by measuring the static pressure at 40 different positions in the chamber. In figure 14 photos are shown of the construction process. The two front chambers are seen in figure 14(*b*) as well as the larger spanwise distributed suction

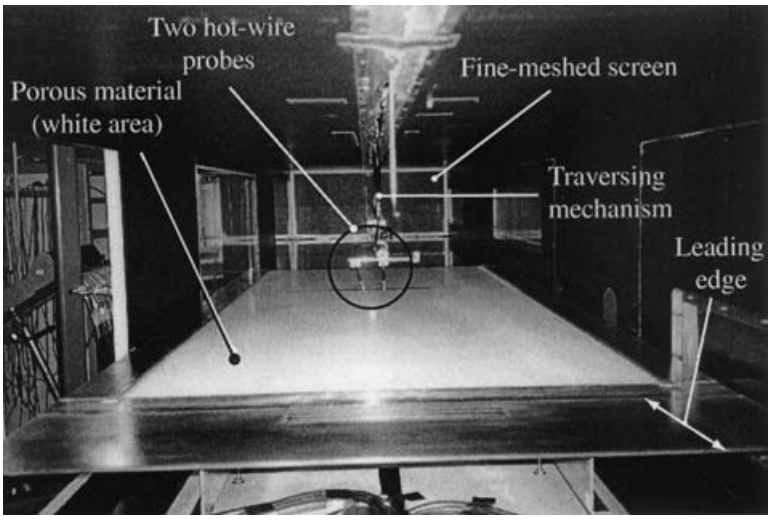

FIGURE 15. Photo of the plate together with the leading edge mounted in the wind tunnel.

holes. Finally, the finished plate mounted in the test section of the MTL wind tunnel is shown in figure 15.

3.4. *Measurement technique*

Single hot-wire probes operating at constant temperature were used to measure the streamwise velocity component. One probe could be traversed in all three spatial directions whereas a second probe was located at a specific spanwise position (in the centre of the tunnel). Both probes were traversed in the x- and y-directions by the same traversing system and their x- and y-positions were the same. This allowed two-point spanwise space correlation measurements.

The single probes were made of 2.5 μm platinum wires with a distance between the prongs of approximately 0.5 mm. The calibration function according to Johansson & Alfredsson (1982) was used, where an extra term is added to King's law to compensate for natural convection which makes it suitable for low-speed experiments:

$$U = k_1\left(E^2 - E_0^2\right)^{1/n} + k_2(E - E_0)^{1/2}. \tag{3.1}$$

4. Experimental results

In the next three subsections the experimental results will be shown and discussed. In the first section the results for the Blasius boundary layer will be presented showing the baseline flow properties and TS-wave experiments. The next section shows the evolution region (from the Blasius to the asymptotic suction state) followed by TS-wave experiments in the asymptotic suction region. Finally FST experiments will be presented where the Blasius and the asymptotic suction results are presented together for direct comparisons.

The experiments reported here were made at a free-stream speed of $5.0\,\mathrm{m\,s^{-1}}$. Since stability experiments are sensitive to the Reynolds number Re, accurate determination of the viscosity is necessary, meaning that both temperature and pressure have to be monitored and measured. For the suction case the suction speed was $1.44\,\mathrm{cm\,s^{-1}}$, corresponding to a pressure difference across the porous plate of $\Delta p = 221\,\mathrm{Pa}$. This

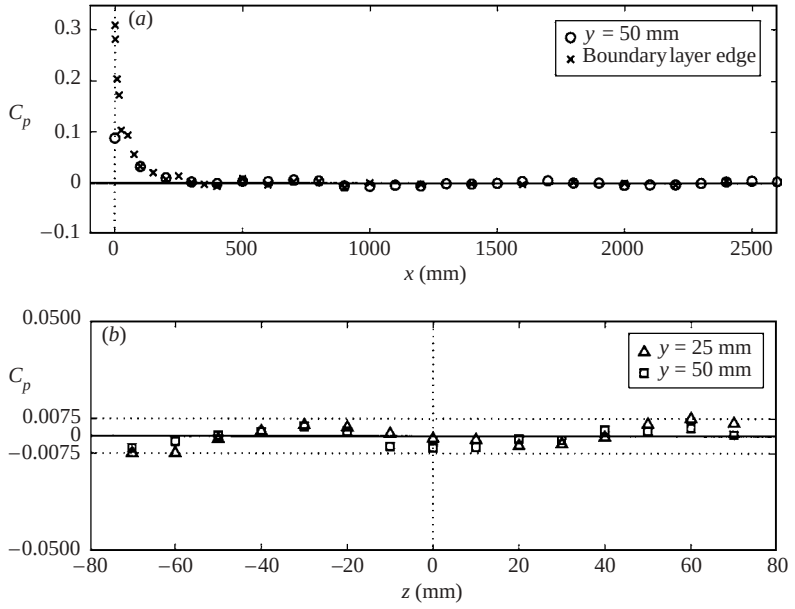

FIGURE 16. Pressure distribution in the test-section. (*a*) Streamwise, and (*b*) spanwise distribution at $x = 300$ mm.

gives an asymptotic boundary layer thickness of 5 mm and a Reynolds number based on the displacement thickness of 347, which corresponds to $C_q = 2.88 \times 10^{-3}$.

4.1. *TS-waves in a Blasius boundary layer*

In order to verify the flow set-up, measurement technique and disturbance generation, the stability characteristics of the Blasius boundary layer for two-dimensional-wave disturbances were determined and compared with previously reported results from the MTL-wind tunnel.

The pressure distribution over the plate was determined by traversing a hot wire close to the plate surface but outside the boundary layer, using the Bernouilli equation to obtain the pressure. This method was used and verified by Klingmann *et al.* (1993) and gives better accuracy than a static pressure tube for low velocities. In figure 16(*a*) the streamwise pressure distribution is plotted for the investigated downstream region on the flat plate. Two different measurements are shown, one at constant y (=50 mm) and the other by traversing the probe to a position just outside the boundary layer. As can be seen there is hardly any difference between the two measurements except at the leading edge, and the variation for $x > 300$ mm is within $\pm 1\%$ of the dynamic pressure. The relatively long pressure gradient region observed in figure 16(*a*) is due to the thickening of the plate due to suction channels and tubing underneath the plate that are present in this experiment. The suction channels alone contribute an extra vertical blockage of 35 mm. In figure 16(*b*) the spanwise pressure distribution is plotted over a spanwise distance of 140 mm at $x = 300$ mm for two different y-positions in the free stream, and is shown to vary within $\pm 0.75\%$ of the dynamic pressure. As expected measured boundary layer profiles for $x = 300$–2400 mm and $z = \pm 70$ mm show excellent agreement with the Blasius profile; for details see Fransson (2001). It is notable that the hot-wire reading very close to the wall is quite accurate, making it possible to measure velocities down to $0.5\,\mathrm{m\,s^{-1}}$ without

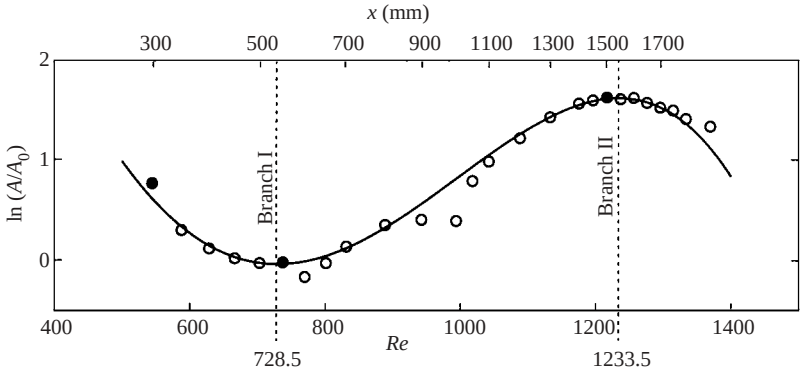

FIGURE 17. Amplitude evolution of the TS-wave at $F = 100$. In this and subsequent figures the symbols are experimental results, and solid lines are the OS-solution of the Blasius profile.

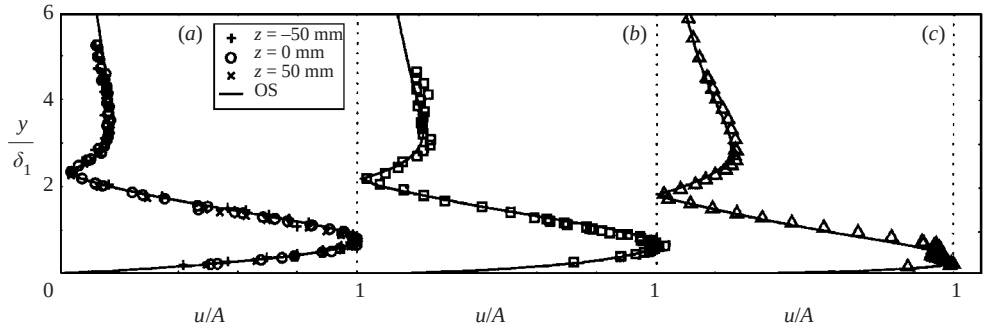

FIGURE 18. Amplitude distribution profiles for $F = 100$. (*a*) $x = 300$ mm at three different spanwise positions ($A = 0.0094$–$0.0097\,\mathrm{m\,s^{-1}}$), (*b*) $x = 550$ mm ($A = 0.0036\,\mathrm{m\,s^{-1}}$), and (*c*) $x = 1500$ mm ($A = 0.0210\,\mathrm{m\,s^{-1}}$).

any deviation from the theoretical curve (cf. figure 1). This is due to the calibration function as well as the low heat conductivity of the porous material.

Controlled stability experiments were performed, where the disturbance to be studied is generated with a known frequency. The first slot located in the leading edge is used to verify the experimental set-up, and the second slot far downstream was used to perform experiments that later will be compared with the TS-wave study in an asymptotic suction boundary layer. In figure 17 the amplitude distribution of the TS-wave at $F = 100$ is shown (in this and following figures A corresponds to the maximum measured amplitude in the profile). The experiment (○) shows good agreement with linear parallel theory (solid line), where both the first and the second branch are well captured by the experiment. The TS-wave is generated at $x = 205$ mm and decays until reaching the first branch at approximately $Re = 728.5$. From there on it grows in amplitude until reaching the second branch at approximately $Re = 1233.5$ where it starts to decay.

In figure 18 the disturbance amplitude distribution profiles are shown corresponding to the three filled symbols (●) in figure 17. In figure 18(*a*) the two-dimensionality of the TS-wave is illustrated by plotting the profiles at three different spanwise positions together with the OS-solution. Parts (*b*) and (*c*) show the smallest (least amplified) and the largest (most amplified) profiles, and in (*b*) (at $x = 550$ mm) the smallness

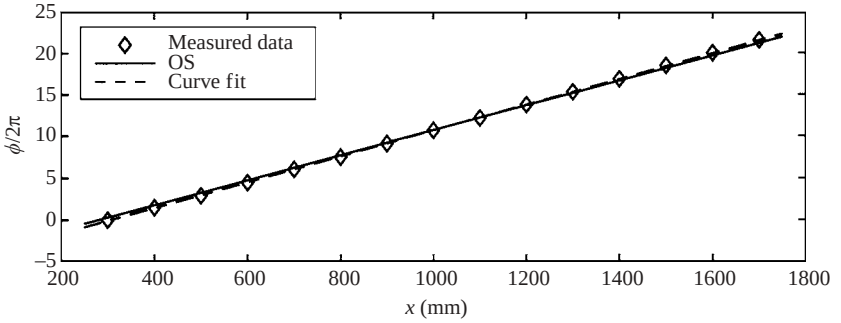

FIGURE 19. Phase distribution in the streamwise direction at $F = 100$.

is revealed near the boundary layer edge where the measured data appear more scattered than in (*c*) (at $x = 1500$ mm). Furthermore, in (*c*) a deformation of the amplitude distribution at the inner maximum can be seen. This deformation has been observed in previous works, see e.g. Klingmann *et al.* (1993) and Ross *et al.* (1970), at downstream distances far from the disturbance source.

The phase velocity ($c = \omega/\alpha_r$) of the wave can be determined simply by determining the real part of the wavenumber (α_r) since the angular frequency (ω) is known. In figure 19 the phase distribution in the streamwise direction is plotted. The phase is taken at the wall-normal distance above the plate where the inner maximum amplitude appears; α_r is then determined by calculating the phase gradient ($\partial\phi/\partial x$), and it is seen to be constant throughout the whole downstream distance investigated. The symbols are experimental data, the solid curve is the OS-solution, and the dashed line is the curve fit for the determination of the gradient. This curve fit gives a phase velocity of $0.34U_\infty$ compared with the theoretical value based on the Blasius profile of $0.36U_\infty$.

From now on all stability results are from the second disturbance slot in the plate located at $x = 1850$ mm corresponding to $Re = 1350$. This is also the region where the stability experiments were performed for the asymptotic suction boundary layer. In figure 20 the amplitude distribution profiles are plotted for $F = 59$ at five different downstream positions. The first x-position closest to the disturbance source, in fact only 50 mm from the source, is not fully developed in the upper part of the profile when compared to the OS-solution. However, from the second x-position the agreement is excellent in this part.

In figure 20 the corresponding phase distribution profiles are also plotted, and they clearly show the phase shift of π radians which can be shown to occur where $\partial v'/\partial y$ changes sign, i.e. at the wall-normal amplitude (v') maxima. The experimental data are in good agreement with the OS-solution (solid line).

For $F = 59$, the TS-wave is unstable in this region, which is between branches I and II. The amplitude growth of the TS-wave is shown in figure 21 together with the amplitude evolution predicted by the OS-equation. The phase velocity is $c = 0.29U_\infty$ determined from figure 22 whereas the corresponding phase velocity obtained from the OS-solution is $c = 0.33U_\infty$. However, the agreement has to be judged as good since there are many external conditions that may influence the result this far downstream from the leading edge. When compared with figure 19 one can observe that the phase velocity is larger just as for the frequency, but in this case the trend is somewhat stronger and the effect is more apparent.

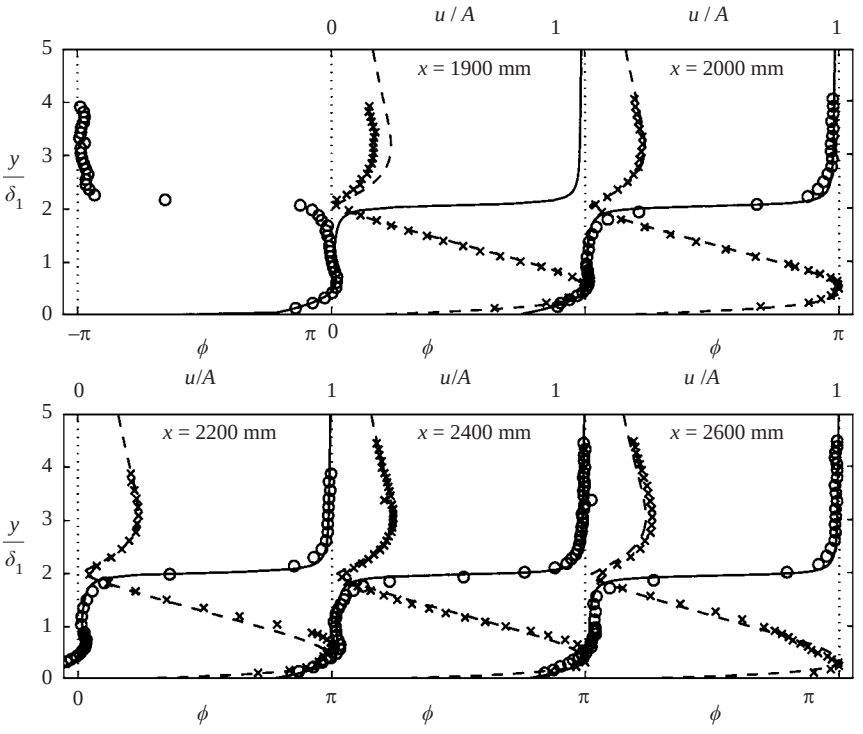

FIGURE 20. Amplitude and phase distribution profiles for $F = 59$ at different x-positions. $\times$ and dashed lines correspond to measured and theoretical amplitude profiles respectively; $\circ$ and solid lines are the corresponding phase profiles.

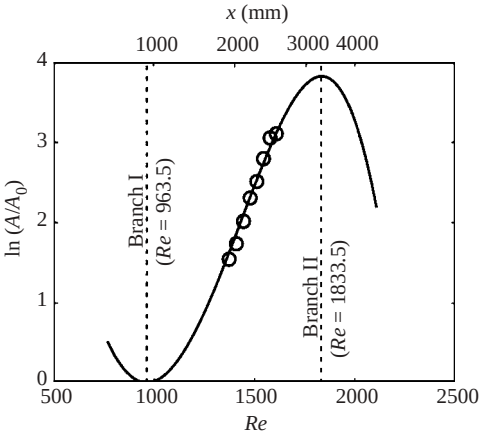

FIGURE 21. Amplitude evolution of the TS-wave at $F = 59$.

Experiments were also performed at two other frequencies ($F = 29$ and $F = 81$) which both showed good agreement with linear stability theory. The latter frequency (at the second slot) is close to the second branch and a clear decay of the amplitude growth was visible. To fit the experimental data to the OS-solution it was necessary to change the Reynolds number. The change corresponds to a virtual (v) origin at

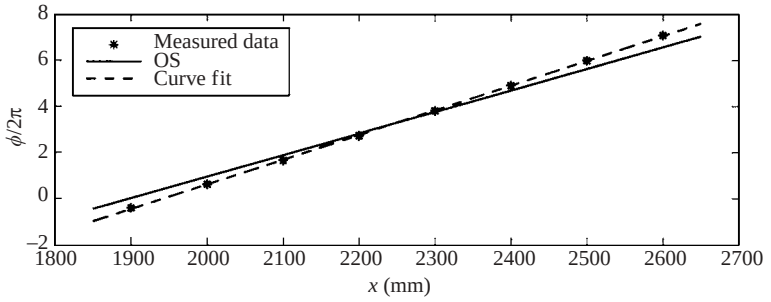

FIGURE 22. Phase distribution in the streamwise direction at $F = 59$.

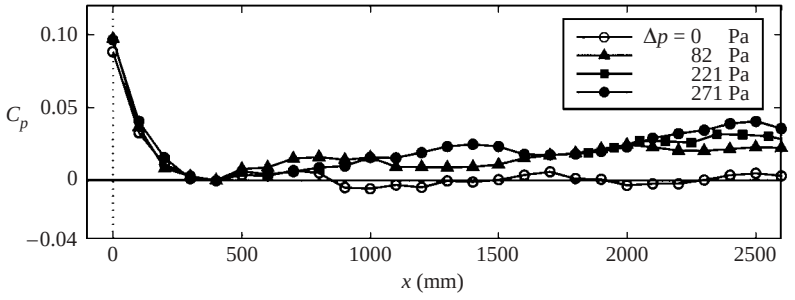

FIGURE 23. Pressure distribution along the streamwise direction for different suction rates. All cases are measured at $y = 50$ mm, and ○ symbols are the same data as in figure 16.

$x_v = -15.8$ mm, which can be considered small (recall the large distance from the leading edge).

In summary the results indicate that the presence of the passive porous plate does not seem to affect the stability characteristics of the boundary layer flow. The amplitude growth of the TS-wave agrees with linear parallel theory as do the amplitude and phase distribution profiles.

4.2. *TS-waves in an asymptotic suction boundary layer*

In this subsection the baseline flow when continuous suction is applied will be presented together with TS-wave experiments in the fully developed asymptotic suction region.

For the present experiments the flat plate and wind tunnel test section were adjusted for zero pressure gradient with no suction through the plate. Much effort was put in to achieving the zero pressure gradient by changing the floor and ceiling positions of the test-section. Recall that the thick plate together with its suction channels and additional blockage due to suction tubing makes the adjustments more difficult. Therefore, no additional geometrical adjustments of the test section were made for the suction case. The result of different suction rates on the pressure distribution in the streamwise direction is shown in figure 23.

All experimental results are for a pressure difference (Δp) over the porous plate of 221 Pa, which corresponds to a suction velocity of 1.44 cm s^{-1} using the permeability value determined through the piston experiment described in § 3.2.

In figure 24 several velocity profiles are plotted in the evolution region, where the wall-normal distance η ($= y\sqrt{U_\infty/x\nu}$) is chosen in order to clearly follow the profile evolution. The development of the boundary layer from the Blasius towards the

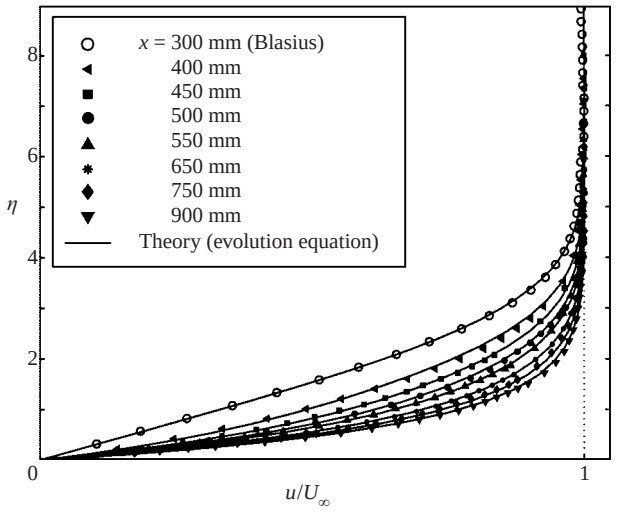

FIGURE 24. Experimental data versus the evolution equation (discussed in § 2.1) in the evolution region. $\eta = y\sqrt{U_\infty/x\nu}$.

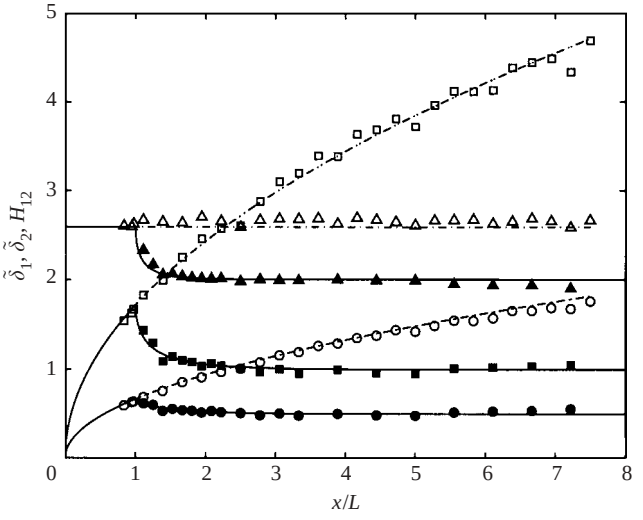

FIGURE 25. Experimental and theoretical results for integral boundary layer parameters. No suction (unfilled) and suction (filled symbols). $\tilde{\delta}_1$ (□) and $\tilde{\delta}_2$ (○) are the displacement and momentum thickness, respectively, normalized with $(UL/\nu)^{1/2}/L$. H_{12} is the shape factor (△). $L = 360$ mm.

asymptotic profile shows good agreement with theory, i.e. the evolution equation, and can be observed in figure 25 (note the scaling). The dash-dotted lines are from the Blasius solution and the solid lines from the evolution equation. L is the impermeable entry length.

The uniformness and two-dimensionality of the flow was checked in the asymptotic suction region by comparing the velocity profiles at different spanwise and downstream positions. There are in total fourteen mean velocity profiles plotted in figure 26, and they show excellent agreement with the theoretical exponential curve (solid line), i.e.

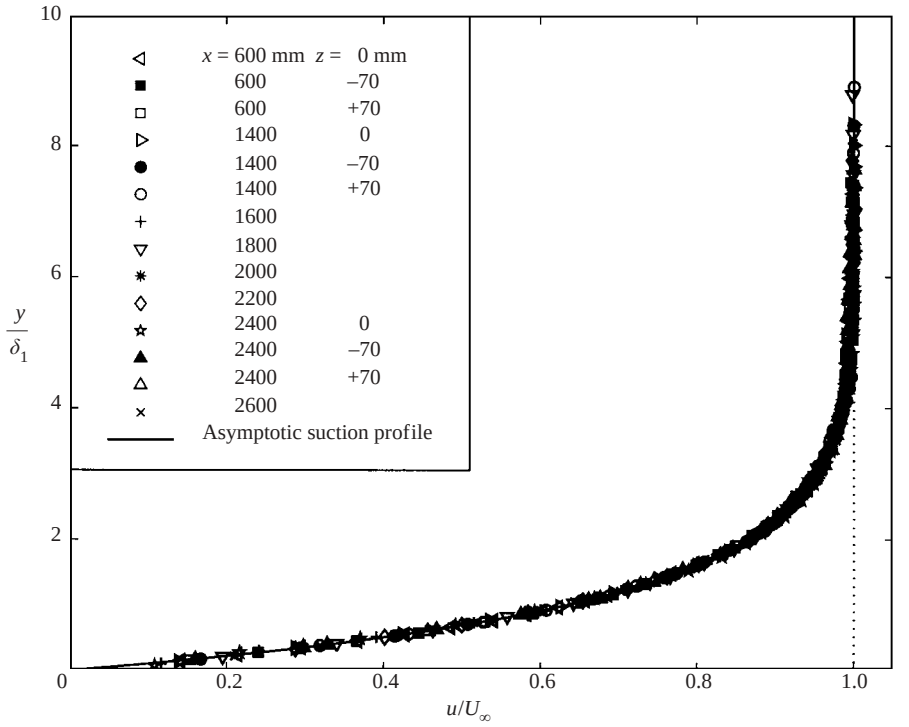

FIGURE 26. Mean velocity profiles for different downstream and some spanwise positions in the asymptotic suction boundary layer.

the analytical asymptotic suction profile. The wall position (y_0) and the displacement thickness (δ_1) were determined by fitting the measured data ($u(y_{\text{meas}})$) to

$$\frac{u(y_{\text{meas}})}{U_\infty} = 1 - \exp(-(y_{\text{meas}} - y_0)/\delta_1) \tag{4.1}$$

by means of the least-square method. This is also a way to verify the suction velocity through the porous plate with the suction velocity corresponding to the pressure difference applied. Since the displacement thickness is $\delta_1 = \nu/V_0$, the suction velocity can easily be calculated once δ_1 is determined from the curve fit. Any profile chosen to verify the suction velocity $1.44\,\text{cm}\,\text{s}^{-1}$ agrees within 9%.

In the TS-wave experiments for the asymptotic suction boundary layer the slot at $x = 1850$ mm was used in order to study the wave in a fully developed boundary layer. However, due to the presence of the slot (50 mm in the streamwise direction) the porous material was made impermeable over the whole spanwise length in order to ensure the two-dimensionality of the flow as was mentioned in § 3.1. This allows the boundary layer to grow slightly and a small increase of δ_1 may be observed downstream of the slot. This results in a Reynolds number increase and for the theoretical comparison $Re = 382$ was used, which was extracted from the profiles. For the present Re the TS-wave will decay rapidly after its generation. In figure 27 the amplitude distribution profiles are shown for different downstream positions. The solid line is the solution from the modified OS-equation and the dotted line is the ordinary OS-equation. Note that the last profile shown is only 350 mm from the disturbance source. Close to the disturbance source the experimental results show

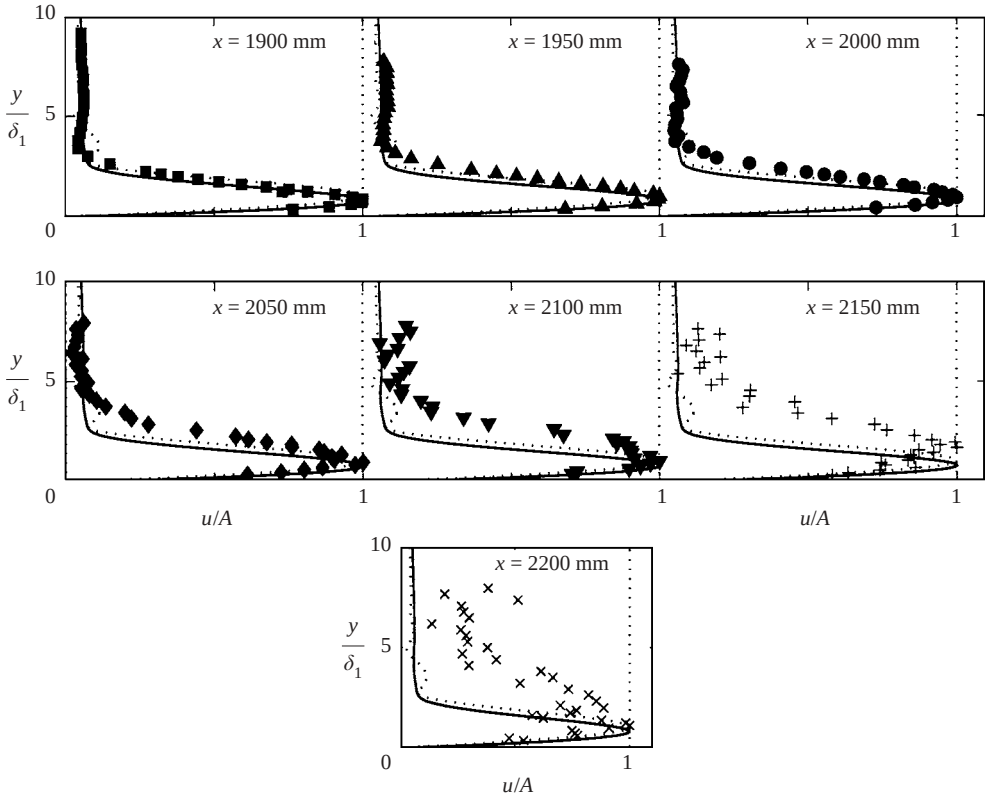

FIGURE 27. Amplitude distribution profiles for different downstream positions in an asymptotic suction boundary layer for $F = 59$. Symbols are measured data, solid lines are the modified OS-solution, and dotted lines the OS-solution.

quite good agreement with the modified OS-solution, whereas further downstream the disturbance is seen to be spread out towards the upper part of the boundary layer and from $x = 2100$ mm the measured data start to appear somewhat scattered. The corresponding phase distribution profiles are plotted in figure 28 with the solid line belonging to the modified OS-solution. The agreement is good in the upper part of the boundary layer and in the free stream, but in the theoretical phase distribution there is a zigzag-formation in the middle of the boundary layer that is not apparent in the experimental results. It is the ratio of the imaginary and real parts of the eigenfunction that determines the shape of the phase distribution and it is a large decrease with a minimum of this ratio at $y/\delta_1 = 2.7$ followed by an increase that gives the zigzag-formation of the theoretical result.

The phase velocity of the TS-wave with $F = 59$ is determined in figure 29. The solid line is the modified OS-solution and this almost corresponds to a curve fit to the measured data. The dotted line is the ordinary OS-solution. The experimental phase velocity is determined to be $c = 0.48U_\infty$, which is the phase velocity predicted by the modified OS-solution.

The amplitude decay is shown in figure 30 together with theoretical results. The theoretical results overpredict the stability of the TS-wave. The experimental result gives a damping factor of $\alpha_i = 0.0153\,\mathrm{mm}^{-1}$, when the first six points are used for the

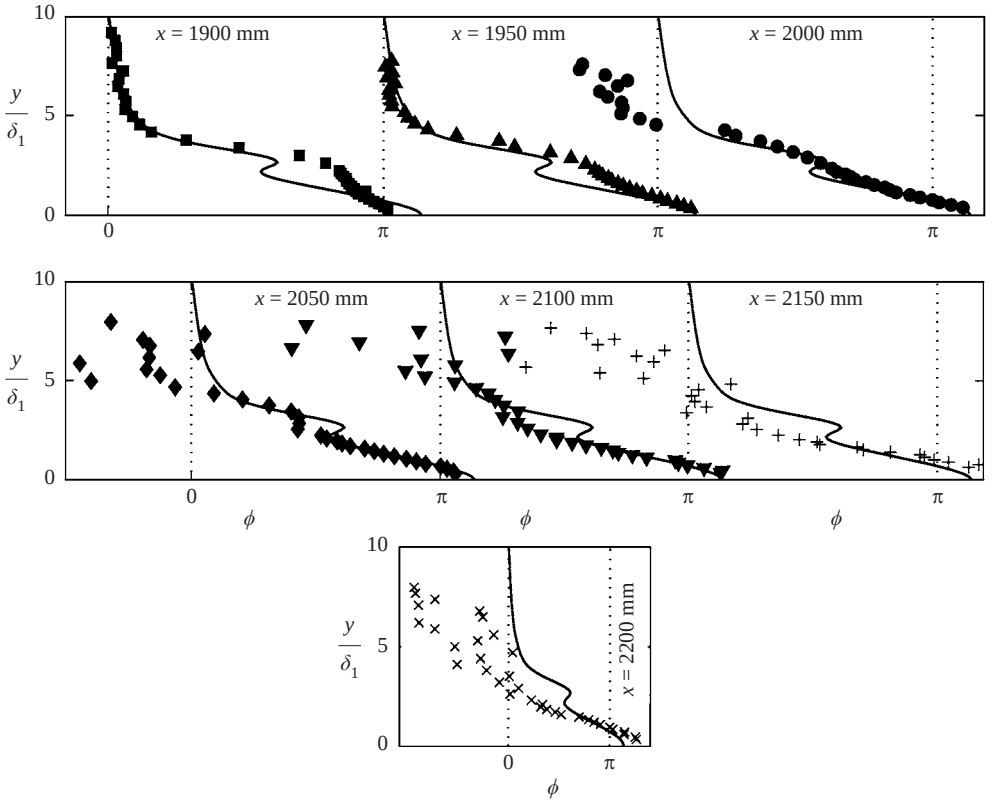

FIGURE 28. Phase distribution profiles corresponding to figure 27.

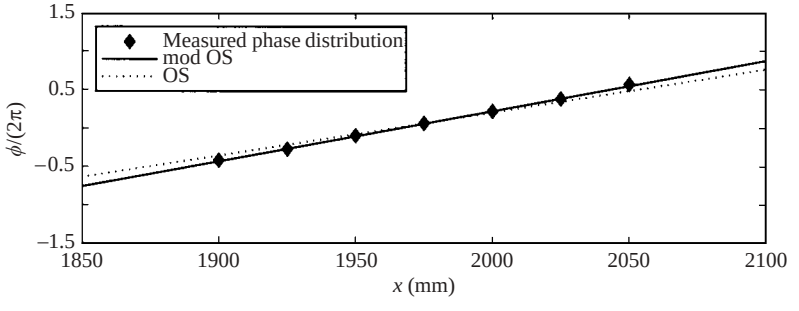

FIGURE 29. Phase distribution in the streamwise direction at $F = 59$ in the asymptotic suction boundary layer.

curve fit, and the modified OS-solution predicts $\alpha_i = 0.0263\,\mathrm{mm}^{-1}$, i.e. a factor 1.72 higher.

TS-wave measurements in the asymptotic suction boundary layer were also made for a higher frequency, $F = 84.4$. The same conclusions can be drawn as for the lower frequency experiment. Good agreement with theory is found for the amplitude distribution profile close to the disturbance source and the theoretical decay factor is still overpredicted compared with the experimental results. Some possible explanations for this discrepancy will be discussed in § 5.

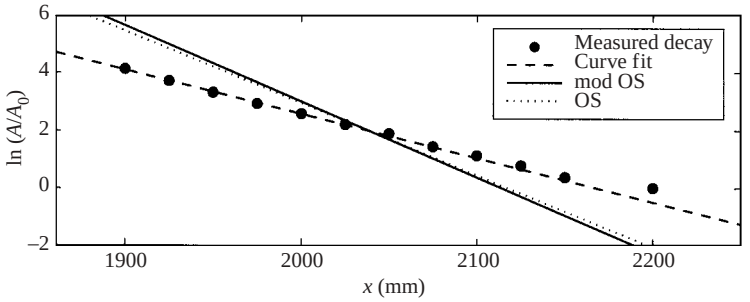

FIGURE 30. Amplitude decay versus the downstream distance for $F = 59$.

4.3. *Experiments with free-stream turbulence*

4.3.1. *Disturbance growth*

Free stream turbulence (FST) gives rise to regions of high and low streamwise velocity (streaky structures) and in a Blasius boundary layer the streamwise disturbance energy grows in linear proportion to the downstream distance. These streaky structures move slowly in the spanwise direction and if the streamwise disturbance amplitude is measured ($u_{\rm rms}$) it is seen to increase with the downstream distance when no suction is applied, whereas in the suction case this amplitude increase was found to be eliminated. This can be observed in figures 31 and 32 where both the mean velocity and disturbance profiles are plotted for both cases, i.e. with and without suction respectively, for the Tu_B-level and for different downstream positions. The position above the plate where the maximum $u_{\rm rms}$-value appears hardly changes in y/δ_1-units and is approximately 1.5; this corresponds to 1/2 and 1/3 of the boundary layer thickness without suction and with suction, respectively. The results are similar for the other two grids (these data can be found in Fransson 2001).

In figure 31(a) the mean velocity profiles hardly show any distortion from the theoretical Blasius profile despite disturbance levels up to 8% inside the boundary layer far downstream. Each solid curve in (b) is a curve fit to data in order to more easily separate the different downstream positions from each other. It is clearly seen that the amplitude increases with increasing x.

For the suction case the mean flow is indistinguishable from the asymptotic suction profile as can be seen in figure 32(a). A large difference is, however, that the disturbance level amplitude inside the boundary layer is much smaller than for the no suction case, and that the level is decreasing slightly with increasing x for the profiles in figure 32(b). Note that the decay is similar to the FST decay observed in the upper part of this figure.

Fransson (2001) reported $v_{\rm rms}$-data obtained from laser Doppler velocimetry measurements both for the Blasius and the suction boundary layers. These results show that in both cases the $v_{\rm rms}$-profiles are similar and decrease monotonically from the free stream towards the wall. This indicates that the suction does not strongly influence the normal velocity fluctuations close to the wall.

In figure 33 the displacement thickness evolution, with and without suction, is plotted versus the downstream distance for different FST intensities. In a Blasius transition region when the profile approaches the turbulent one an increase in the displacement thickness is expected. According to this figure the displacement thickness seems to increase somewhat in both the suction and no suction case when the Tu-level

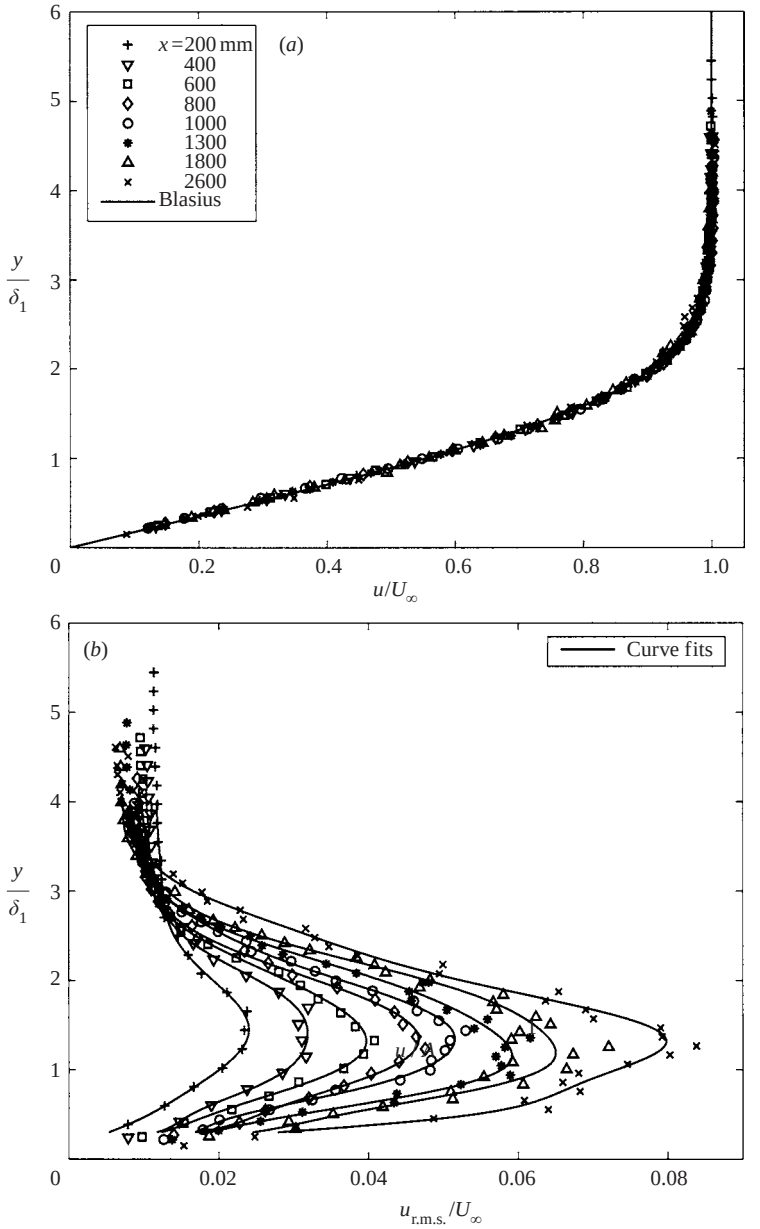

FIGURE 31. Data for different downstream positions from grid B without suction. (*a*) Mean velocity profiles, and (*b*) u_{rms}-profiles for the same x-positions as in (*a*).

is increased. The dashed and solid lines in figure 33 correspond to the theoretical laminar δ_1-evolution of the Blasius and the suction case, respectively.

In figure 34 the disturbance amplitude, here chosen as the maximum value of the disturbance profiles, for the three different grids is plotted versus the downstream distance from the leading edge. For the no suction cases the disturbance amplitude has been found to grow in proportion to $x^{1/2}$ and a similar development is observed here. For grid B transition does not occur over the length of the measured region,

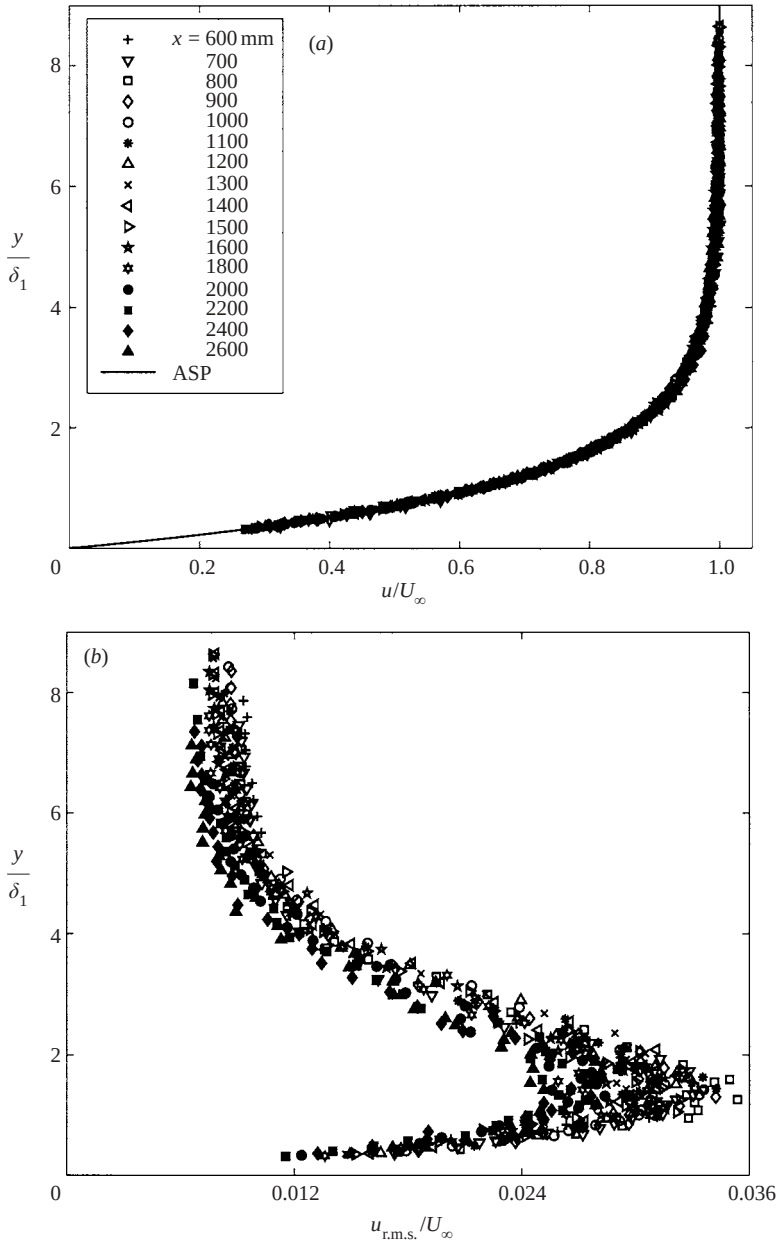

FIGURE 32. As figure 31 but with suction through the porous plate.

despite the fact that the u_{rms}-level is above 8% at the end. For high enough Tu-levels the FST will force the flow to transition. For grid G a maximum of nearly 17% in the turbulence intensity is found at $x \approx 1800$ mm. Such a maximum is usually observed in the intermittent region where the flow consists both of laminar regions and turbulent spots. Further downstream the intensity decreases, which is expected when the flow goes towards a fully developed turbulent stage. For grid E, measurements were only made up to $x = 700$ mm where a similar high level was observed.

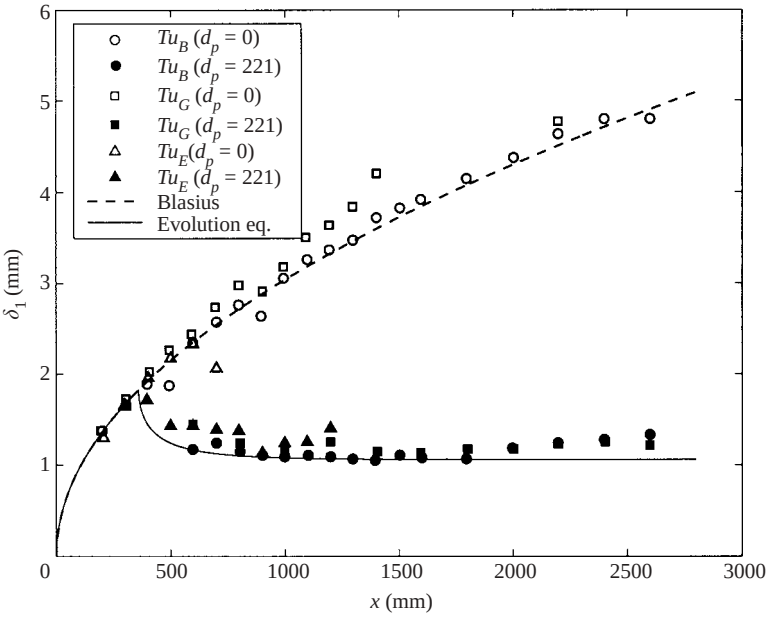

FIGURE 33. The displacement thickness evolution with and without suction when influenced by FST.

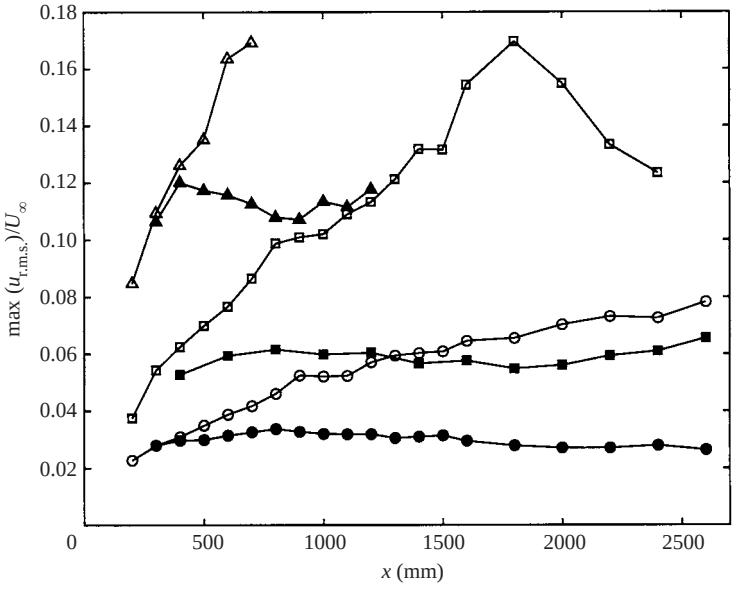

FIGURE 34. Peak disturbance amplitude vs downstream distance from the leading edge. No suction (unfilled) and suction (filled symbols). ○, Tu_B; □, Tu_G; △, Tu_E.

When applying the present rate of suction it is found that transition does not occur for any of the grids, although the mean velocity profiles deviate from the asymptotic profile at the most downstream positions for grid E. Instead the fluctuation level inside the boundary layer reaches an almost constant level for all three grids and the level is in each case close to that where the suction starts. An interesting observation

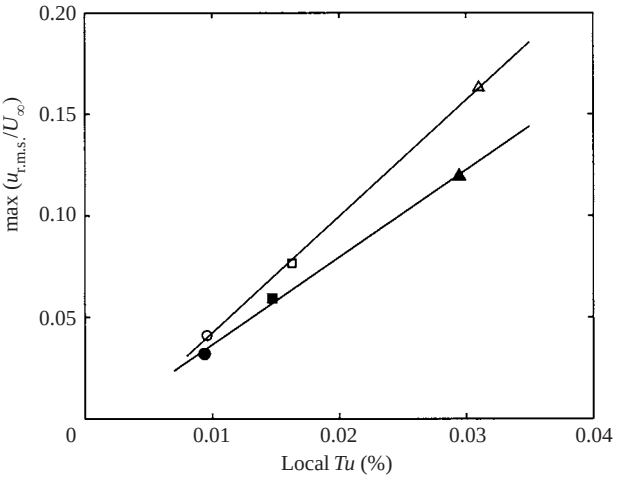

FIGURE 35. The maximum $u_{\rm rms}$-value versus the local Tu at $x = 600$ mm. (○) $Tu_{\rm B}$, (□) $Tu_{\rm G}$ and (△) $Tu_{\rm E}$. Filled symbols with suction and unfilled without.

is that this level is proportional to the level of the FST. This is shown in figure 35 where the maximum $u_{\rm rms}$-values (or constant level in the suction case) versus the local Tu-level are plotted for both the suction and no suction case.

The data presented in figure 34 appear somewhat scattered and another way to plot the disturbance evolution is to evaluate the average disturbance energy (E_u) by integrating $u_{\rm rms}^2$ across the boundary layer. This measure is plotted in figure 36 versus the downstream distance from the leading edge. The figures show the well-known linear growth of the disturbance energy with the downstream distance for the no suction case and for all Tu-levels. In the case with suction the energy growth ceases and a more or less constant level for each grid is obtained.

4.3.2. *Spanwise scale of the streaks*

The spanwise scale of the streaks can be determined through two-point correlation measurements of the streamwise velocity component. It is well known that the position where the streamwise correlation coefficient ($R_{\rm uu}$) shows a distinct minimum can be interpreted as half the dominating spanwise wavelength of the streaks (see e.g. Matsubara & Alfredsson 2001), and will from here on be denoted $\lambda_z^{1/2}$. In order to determine this spanwise scale the correlation measurement should preferably be done inside the boundary layer where the maximum $u_{\rm rms}$ appears, as this is the position where the correlation coefficient will appear strongest. The spanwise correlation coefficient is defined as

$$R_{uu} = \frac{\overline{u(z)u(z+\Delta z)}}{\overline{u(z)^2}}.$$

In figure 37 two correlation measurements are shown, one measured at the boundary layer edge (●) and the other where the maximum $u_{\rm rms}$ appears (○). In the former the correlation is close to one at the first measuring point and it decays gradually to become uncorrelated far away. In the latter measurement the correlation coefficient shows the (previously mentioned) distinct minimum. An interesting observation is the zero crossing of the correlation coefficient, which will be shown to be as good a measure of the spanwise scale of the streaks as the minimum value. In figure 38 the correlation coefficient is plotted for gradually increasing distance (y) from the plate.

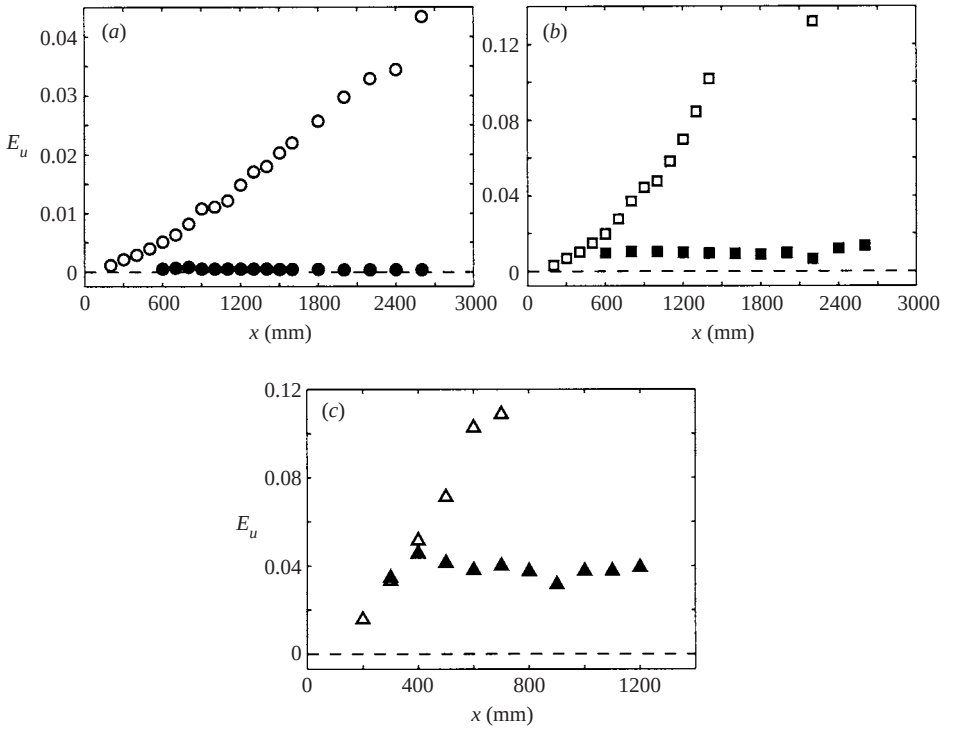

FIGURE 36. The growth of the average disturbance energy inside the boundary layer, defined as $E_u = (1/\delta U_\infty^2) \int_0^\delta u_{\rm rms}^2 \, {\rm d}y$ (where δ is the boundary layer thickness). (*a*) $Tu_{\rm B}$, (*b*) $Tu_{\rm G}$, and (*c*) $Tu_{\rm E}$.

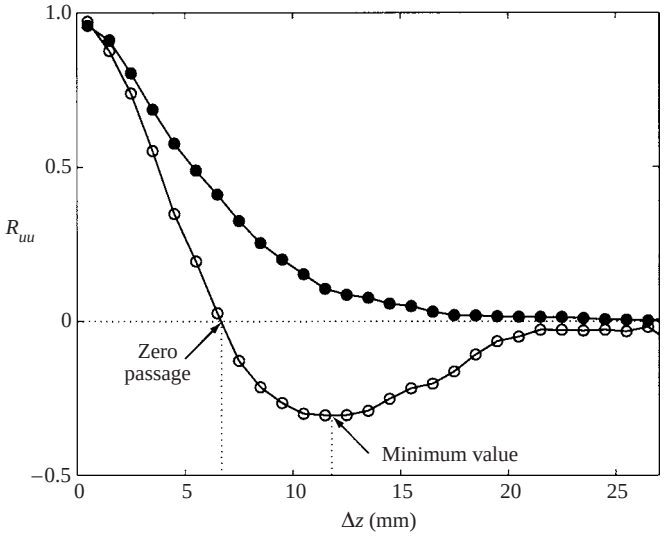

FIGURE 37. The spatial (spanwise) correlation coefficient (R_{uu}) versus the separation distance (Δz). ●, Measured at the boundary layer edge, and ○, measured at the position inside the boundary layer where the maximum $u_{\rm rms}$ appears. The two curves are obtained from smoothed data from a (y, z)-plane measurement at $x = 1800$ mm with $Tu_{\rm B}$.

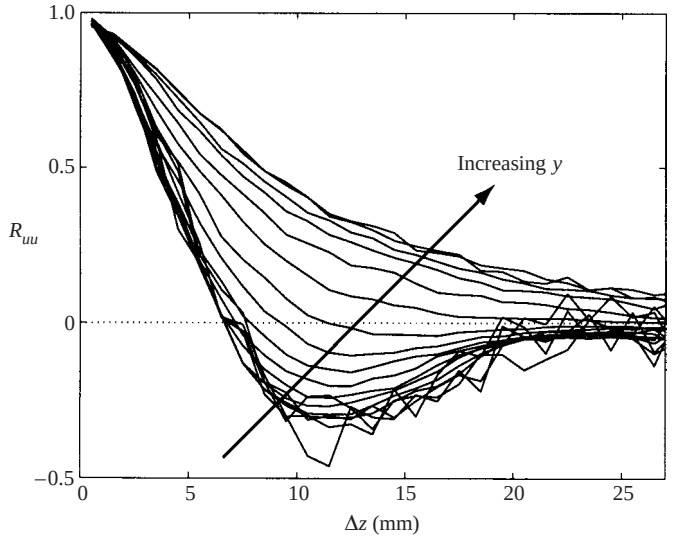

FIGURE 38. The spatial (spanwise) correlation coefficient (R_{uu}) versus the separation distance (Δz) for different distances above the plate at $x = 1800$ mm with Tu_B.

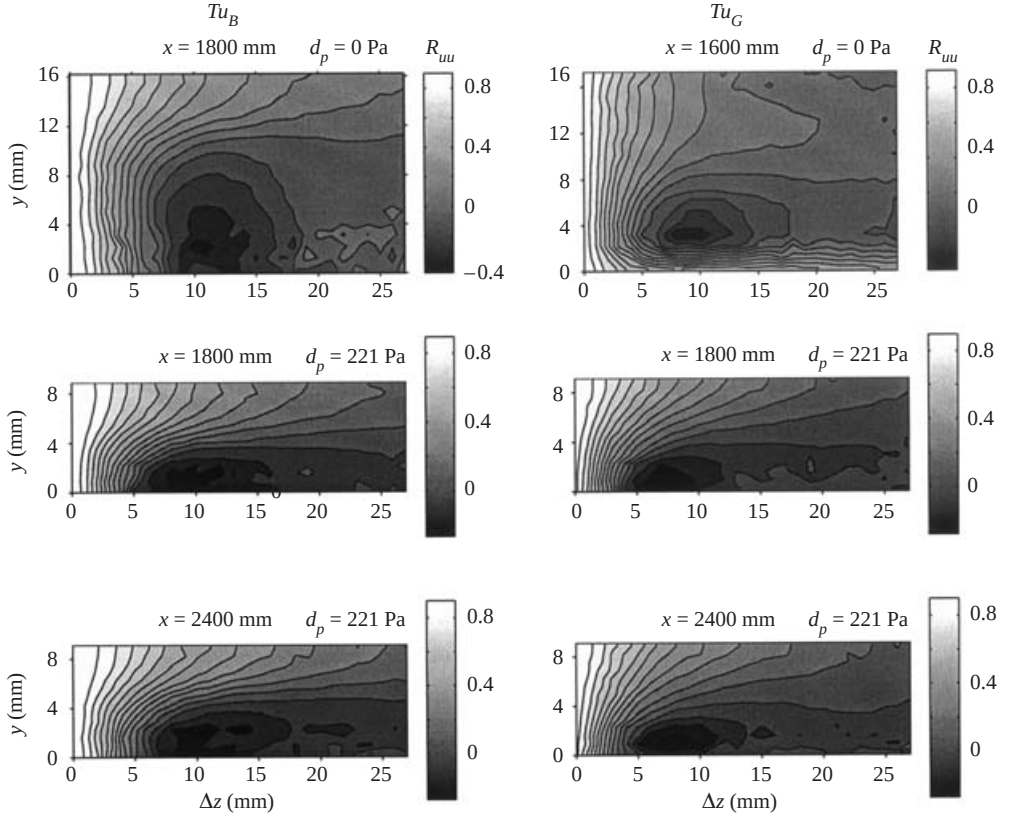

FIGURE 39. Contour plots of R_{uu} in the (y, z)-plane for different downstream positions for Tu_B (left) and Tu_G (right). The no suction case consists of 504 measurement points and the suction case of 392. $\delta_{0.99} \approx 11$ and 5 mm for $d_p = 0$ and 221 Pa respectively.

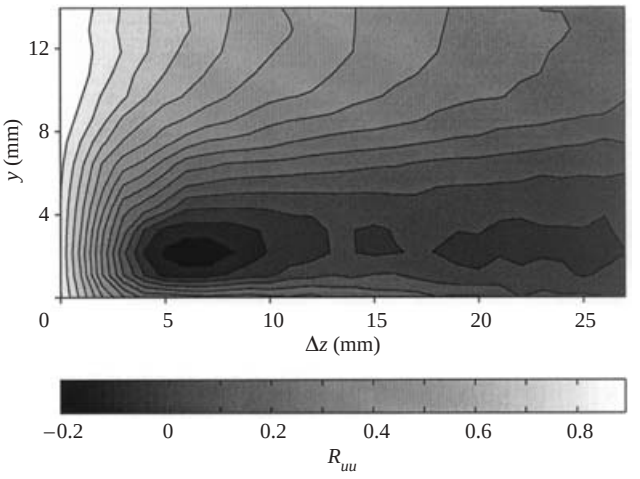

FIGURE 40. Contour plot of R_{uu} in the yz-plane at $x = 500$ mm with Tu_E and suction. Total number of measurement points is 392.

Close to the surface the data seem to be somewhat scattered, which is due to the short sampling time (30 s). From data such as shown in figure 38 one can draw a contour plot in the (y, z)-plane for an overview of the structure inside the boundary layer. This was done for different Tu-levels and x-positions with and without suction and is shown in figure 39 (for Tu_B and Tu_G) and 40 (for Tu_E with suction). Figure 39 shows that the spanwise scale of the streaky structures is only slightly decreased by suction, despite a twofold reduction in boundary layer thickness. This indicates that disturbances inside the boundary layer are strongly dependent on the scale of the FST. Note that the minimum value is clearly distinguishable in all cases, including figure 40 with Tu_E at $x = 500$ mm.

Matsubara & Alfredsson (2001) showed that the spanwise scale of the streaks observed near the leading edge seems to depend on the FST scales introduced into the boundary layer at an early stage of the receptivity process. Further downstream this scale seems to adapt to the boundary layer thickness and grows in proportion to this thickness. In the suction case the scenario is slightly different since the spanwise scale is hardly changed compared to the spanwise scale observed in the Blasius boundary layer, despite the fact that the boundary layer thickness is only half of that in a Blasius layer. This result was obtained for all three FST intensities tested. The conclusion from figure 39 is that the effect of suction on the streaks is compression, i.e. since the boundary layer thickness decreases the streaks are compressed in the wall-normal direction but the spanwise scale is preserved. This creates a wider structure in terms of boundary layer thickness compared to the Blasius case.

In figure 41 the evolution of the spanwise scales of the streaks from all three grids are shown. The minimum values of the correlation coefficient (R_{uu}) were determined by fitting a third-order polynomial to the measured data and the zero crossing of R_{uu} by fitting a second-order polynomial. For all cases there is a tendency for the scales to increase with x; however the effect is strongest for grid B (figure 41*a*). If there is a difference between the no suction and suction cases, a tendency towards a slower growing spanwise scale in the suction case compared to the no suction case may be observed. The spanwise scale of the streaks seems to decrease with increasing FST intensities according to figure 41. As can be seen in figure 41(*d*) the zero crossing is an

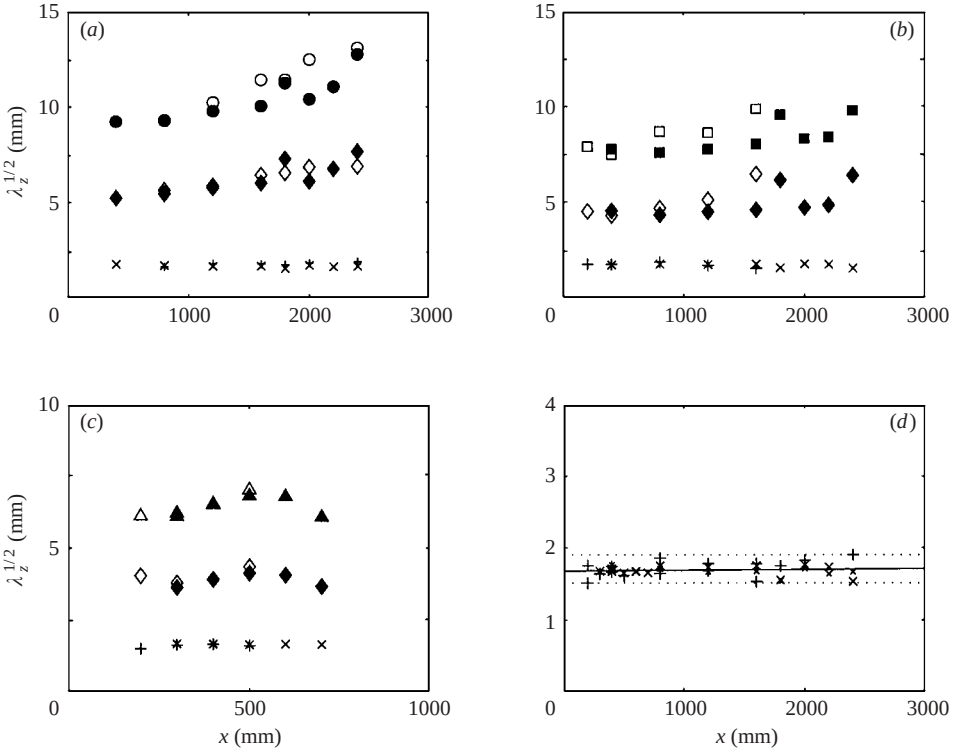

FIGURE 41. Evolution of the spanwise scale of the streaks. No suction (unfilled) and suction (filled symbols). (*a*) ○, min(R_{uu}) and ◆, zero(R_{uu}) for Tu_B. (*b*) □, min(R_{uu}) and ◆, zero(R_{uu}) for Tu_G. (*c*) △, min(R_{uu}) and ◇, zero(R_{uu}) for Tu_E. (*d*) min(R_{uu})/zero(R_{uu}) for all grids: +, no suction and ×, suction.

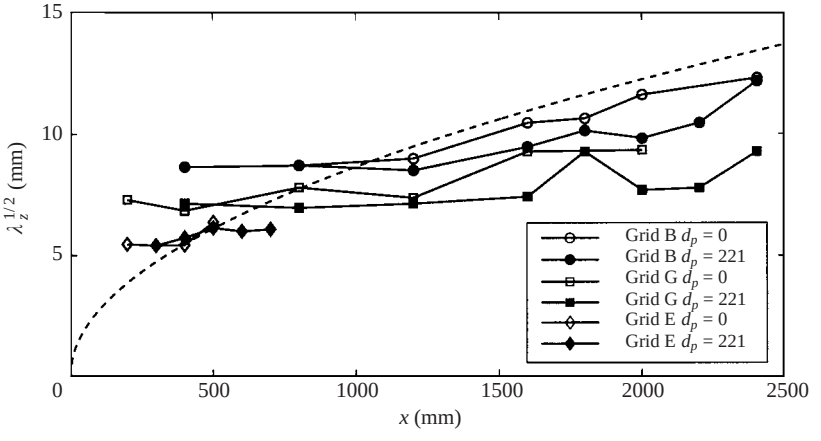

FIGURE 42. Evolution of the spanwise scale of the streaks for all cases plotted together with the Blasius boundary layer thickness evolution (dashed line). Same data as in figure 41.

equally good measure of the spanwise scale as the minimum value of the correlation coefficient. The zero crossing cannot have a direct physical interpretation, but is easier to determine from an experimentalist's point of view. All ratios of the minimum value

of the correlation coefficient and the zero crossing of the present data collapse at a value of 1.68 ± 0.23.

In figure 42 the evolution of the spanwise scales of the streaks is plotted again (same data as in figure 41) together with the Blasius boundary layer thickness evolution. This figure allows a direct comparison between all cases and confirms previous studies, see e.g. Matsubara & Alfredsson (2001), that the spanwise scale comes close to the boundary layer thickness for low *Tu*-levels in the Blasius boundary layer.

5. Discussion and summary

In the present work a successful experimental set-up to establish the asymptotic suction boundary layer in a wind tunnel is described. The main interest of the study is not to develop a practical suction set-up but to establish a generic flow situation where the effect due to suction on disturbance development inside the boundary layer can be investigated. The suction coefficient C_q is fairly high compared to that given in the literature as a reasonable value for flow control.

A test plate with a porous surface material was constructed and had a specially designed leading edge with a short region of non-zero pressure gradient. The mean flow development from the leading edge of the plate is shown to be in good agreement with a theoretical boundary layer analysis and when the asymptotic suction region is reached there is an excellent agreement between the theoretical and experimental boundary layer profiles.

The stability equations for modal disturbances are derived where the wall-normal mean velocity modifies the standard OS-equation. The effect of this component as well as the change in mean velocity profile is discussed, and it is shown that the main effect is due to the profile change.

TS-waves are generated in the experiment through a spanwise slot and the development of the waves over the plate without suction is shown to be in good agreement with standard stability theory and previous experiments. The same conclusion can be drawn for the asymptotic suction boundary layer although in that case the waves are strongly damped. The correspondence between the streamwise amplitude profiles and the phase velocity is good, but the decay factor predicted by linear stability theory is slightly overestimated compared to the experimental results. It is not clear why this difference occurs but four main possibilities for the discrepancy have been identified, namely (i) the adverse pressure gradient, (ii) the disturbance introduced by the width of the slot which may give small deviations of the mean profile, (iii) the low wave amplitude, and (iv) a possible obliqueness of the measured disturbance. The adverse pressure gradient that is present in the asymptotic suction region (due to the suction, see figure 23), influences the stability characteristics in such a way that the flow would be less stable. This would bring the theoretical results closer to the experimental ones. However, the pressure gradient is small and PSE calculations with the present pressure gradient, show hardly any effect on the stability characteristics (A. Hanifi, private communication).

Secondly, the profile is affected by the impermeable streamwise length of 50 mm in connection with the disturbance slot. Suddenly stopping the continuous suction over some streamwise distance would allow the boundary layer to grow and the profiles to become slightly disturbed when passing above the impermeable slot. It is well known that even small deviations can give large differences in the decay rate. Also the displacement thickness becomes larger, as noted in the measurements. However, this latter effect was taken into account in the stability calculations by using a higher

Reynolds number of $Re = 382$ that was extracted from the profiles in the region of interest.

Thirdly, one cannot rule out the possibility that the small amplitude of the wave disturbances in the experiment may make the measurements susceptible to noise. This would increase the measured level, especially at the more downstream positions, thereby giving a too low decay rate.

Finally, even though the generated disturbance is two-dimensional the external disturbances and high noise level may cause an oblique mode which is less stable than the corresponding two-dimensional disturbance. Three-dimensional disturbance analysis reveals that the theoretical disturbance growth approaches the experimental one as β increases (equal at around $\beta = 0.25$). However, this mode has a phase velocity of $0.70U_\infty$ (compared to $0.48U_\infty$) which in turn simply moves the mismatch to the phase velocity. Despite this, an obliqueness cannot be excluded as a possible factor. A combination of all the suggested explanations is the most likely scenario, making the situation rather complicated.

The second part of this study deals with the development of FST-induced disturbances. Direct comparisons between the no suction (Blasius) and suction cases were made. In the no suction case the results were similar to earlier work, showing a linear growth of the disturbance energy in the downstream direction until spot formation occurs. However, in the suction case the growth of the disturbance amplitude has been shown to cease, and the present amplitude level is essentially constant throughout the measured region for this particular suction velocity. In consequence, transition is inhibited for all cases with suction. The 'constant' level was found to be proportional to the FST level. Note that for larger suction rates the disturbance amplitude decays, and for smaller rates the growth is simply damped (cf. Yoshioka, Fransson & Alfredsson 2003).

The spanwise scale of the streaks is maintained when suction is applied like the no suction case, despite a twofold boundary layer thickness reduction. In both cases the receptivity process at the leading edge is similar, due to the Blasius boundary layer that develops through the impermeable entry length for both the suction and the no suction case. This might explain the development of similar spanwise scales in the two studied cases since the initial spanwise scale is probably set by the receptivity process.

The spanwise wavenumber of the optimal perturbation in a Blasius boundary layer is at $\beta = 0.775$ when normalized with the displacement thickness (see e.g. Andersson, Berggren & Henningson 1999 and Luchini 2000). For the asymptotic suction boundary layer the optimum is at $\beta = 0.53$ (Fransson & Corbett 2002), i.e. a somewhat widened structure inside the boundary layer compared to the Blasius case. This is in agreement with the present experiments even though the experiment shows even more widened structures inside the boundary layer for low FST levels (see figure 39). In some recent papers (Andersson *et al.* 1999; Luchini 2000; Matsubara & Alfredsson 2001) comparisons have been made between the optimal perturbation theory and experiments at $Tu = 1.5\%$. The streamwise disturbance profiles were found to agree well, but initially there is a mismatch in the spanwise wavelength of the streaks as pointed out by Matsubara & Alfredsson (2001). The results of Fransson & Corbett (2002) show similarly good agreement for the asymptotic boundary layer also for the disturbance distribution normal to the wall.

The experimental and theoretical results support the following hypothesis. When FST of a sufficient level is present, disturbances, which develop into streaks, are triggered inside the boundary layer. The scale of the triggered disturbances depends

on both the level and the scale of the FST. Higher FST level implies that more energy is present over the whole range of scales (see figure 6). A certain level is needed to generate disturbances within a certain scale interval, but if this level is high enough the boundary layer would preferably amplify disturbances whose scales are close to that of the optimal disturbance. This is in accordance with the experiments, which clearly show that the spanwise scale of the streaks decreases with increasing level of FST (as shown in figure 41), approaching the scale given by optimal perturbation theory. For instance for the Blasius boundary layer in the range $x = 200$–500 mm the streak spacing ($\lambda_z^{1/2}$) is between 6 and 7.5 mm when subjected to Tu_E (see figure 41*c*) where the theory gives $\lambda_z^{1/2} = 5.4$–8.5 mm.

Finally one should bear in mind that for transition it is not only the streak amplitude and scale that is important. The streaks will not break down to turbulence without the development of a secondary instability. The triggering of the secondary instability may be due to the FST acting on top of the streaks. In order to obtain a growing instability the streak amplitude must be sufficiently large. With the suction rate of the present experiments it seems that the amplitude of the streaks is not high enough for the secondary instability to be able to trigger breakdown to turbulence.

We wish to thank Mr Marcus Gällstedt at the Department of Mechanics at KTH for his skillful construction work of the leading edge. This work has been financially supported by The Swedish Research Council (VR) which is gratefully acknowledged.

REFERENCES

Andersson, P., Berggren, M. & Henningson, D. S. 1999 Optimal disturbances and bypass transition in boundary layers. *Phys. Fluids* **11**, 134–150.

Andersson, P., Brandt, L., Bottaro, A. & Henningson, D. S. 2001 On the breakdown of boundary layer streaks. *J. Fluid Mech.* **428**, 29–60.

Bertolotti, F. P. 1991 Linear and nonlinear stability of boundary layers with streamwise varying properties. PhD thesis, The Ohio State University, Department of Mechanical Engineering, Columbus, Ohio.

Drazin, P. G. & Reid, W. H. 1981 *Hydrodynamic Stability*. Cambridge University Press.

Elofsson, P. 1998 Experiments on oblique transition in wall bounded shear flows. PhD thesis, KTH, Stockholm; *TRITA-MEK Tech. Rep.* 1998:05.

Fasel, H. & Konzelmann, U. 1990 Non-parallel stability of a flat-plate boundary layer using the complete Navier–Stokes equations. *J. Fluid Mech.* **221**, 311–347.

Fransson, J. M. M. 2001 Investigations of the asymptotic suction boundary layer. *TRITA-MEK Tech. Rep.* 2001:11; Licentiate Thesis, KTH, Stockholm. Also available at www.mech.kth.se.

Fransson, J. H. M. & Alfredsson, P. H. 2003 On the hydrodynamic stability of channel flow with cross flow. *Phys. Fluids* **15**, 436–411.

Fransson, J. H. M. & Corbett, P. 2002 Optimal linear growth in the asymptotic suction boundary layer. *Eur. J. Mech.* B/*Fluids* (Submitted).

Fransson, J. H. M. & Westin, K. J. A. 2001 Errors in hot-wire X-probe measurements induced by unsteady velocity gradients. *Exps. Fluids* **32**, 413–415.

Gregory, N. 1961 Research on suction surfaces for laminar flow. *Boundary Layer and Flow Control* **II**, 924–957.

Gustavsson, C. 2000 Development of three-dimensional disturbances in boundary layers with suction. Master Thesis, Luleå University of Technology, Luleå.

Haj-Hariri, H. 1988 Transformations reducing the order of the parameter in differential eigenvalue problems. *J. Comput. Phys.* **77**, 472–484.

Hocking, L. M. 1975 Non linear instability of the asymptotic suction velocity profile. *Quart. J. Mech. Appl. Maths* **28**, 341–353.

Jacobs, R. G. & Durbin, P. A. 2001 Simulations of bypass transition. *J. Fluid Mech.* **428**, 185–212.

Johansson, A. V. & Alfredsson, P. H. 1982 On the structure of turbulent channel flow. *J. Fluid Mech.* **122**, 295–314.

Jones, C. W. & Watson, E. J. 1963 Two-dimensional boundary layers. In *Laminar Boundary Layers* (ed. L. Rosenhead). Oxford University Press.

Joslin, R. D. 1998 Aircraft laminar flow control. *Annu. Rev. Fluid Mech.* **30**, 1–29.

Kendall, J. M. 1985 Experimental study of disturbances produced in a pre-transitional laminar boundary layer by weak free stream turbulence. *AIAA Paper* 85-1695.

Klingmann, R. G. B., Boiko, A. V., Westin, K. J. A., Kozlov, V. V. & Alfredsson, P. H. 1993 Experiments on the stability of Tollmien–Schlichting waves. *Eur. J. Mech.* B/*Fluids* **12**, 493–514.

Landahl, M. T. 1980 A note on an algebraic instability of inviscid parallel shear flows. *J. Fluid Mech.* **98**, 243–251.

Lindgren, B. & Johansson, A. V. 2002 Evaluation of the flow quality in the MTL wind-tunnel. *TRITA-MEK Tech. Rep.* 2002:13, KTH, Stockholm.

Luchini, P. 2000 Reynolds number independent instability of the boundary layer over a flat surface: optimal perturbations. *J. Fluid Mech.* **404**, 289–309.

Lundell, F. 2000 Streak breakdown and transition control in wall-bounded flows. *TRITA-MEK Tech. Rep.* 2000:06; Licentiate Thesis, KTH, Stockholm.

MacManus, D. G. & Eaton, J. A. 2000 Flow physics of discrete boundary layer suction-measurements and predictions. *J. Fluid Mech.* **417**, 47–75.

Matsubara, M. & Alfredsson, P. H. 2001 Disturbance growth in boundary layers subjected to free-stream turbulence. *J. Fluid Mech.* **430**, 149–168.

Morkovin, M. V. 1969 The many faces of transition. In *Viscous Drag Reduction* (ed. C. S. Wells), pp. 1–31. Plenum.

Myose, R. Y. & Blackwelder, R. F. 1995 Control of streamwise vortices using selective suction. *AIAA J.* **33**, 1076–1080.

Orszag, S. A. & Patera, A. 1983 Secondary instability in wall-bounded shear flows. *J. Fluid Mech.* **128**, 347–385.

Pfenninger, W. & Groth, E. 1961 Low drag boundary layer suction experiments in flight on a wing glove of an F-94A airplane with suction through a large number of fine slots. *Boundary Layer and Flow Control* **II**, 981–999.

Poll, D. I. A., Danks, M. & Davies, A. J. 1992*a* The effect of surface suction near the leading edge of a swept-back wing. *First European Forum on Laminar Flow Technology, 16–18 March 1992, Hamburg, Paper* 92-01-029. *DGLR-Bericht* 92-06, pp. 278–293.

Poll, D. I. A., Danks, M. & Humphreys, B. E. 1992*b* The aerodynamic performance of laser drilled sheets. *First European Forum on Laminar Flow Technology, 16–18 March 1992, Hamburg, Paper* 92-01-028. *DGLR-Bericht* 92-06, pp. 274–277.

Reshotko, E. 2001 Transient growth: A factor in bypass transition. *Phys. Fluids* **13**, 1067–1075.

Reynolds, G. A. & Saric, W. S. 1986 Experiments on the stability of the flat-plate boundary layer with suction. *AIAA J.* **24**, 202–207.

Rheinboldt, W. 1956 Zur Berechnung stationärer Grenzschichten bei kontinuierlicher Absaugung mit unstetig veränderlicher Absaugegeschwindigkeit. *J. Rat. Mech. Anal.* **5**, 539–604.

Roberts, P. J. D., Floryan, J. M., Casalis, G. & Arnal, D. 2001 Boundary layer instability induced by surface suction. *Phys. Fluids* **13**, 2543–2552.

Ross, J. A., Barnes, F. H., Burns, J. G. & Ross, M. A. 1970 The flat plate boundary layer. Part 3. Comparison of theory and experiments. *J. Fluid Mech.* **43**, 819–832.

Schlichting, H. 1979 *Boundary Layer Theory*. McGraw-Hill.

Schmid, P. J. & Henningson, D. S. 2001 *Stability and Transition in Shear Flows*. Springer.

Schubauer, G. B. & Skramstad, H. K. 1948 Laminar boundary layer oscillations and transition on a flat plate. *Tech. Rep.* 909. NACA.

Taylor, G. I. 1971 A model for the boundary condition of a porous material. Part 1. *J. Fluid Mech.* **49**, 319–326.

Westin, J. 1997 Laminar-turbulent boundary layer transition influenced by free stream turbulence. PhD thesis, KTH, Stockholm; *TRITA-MEK Tech. Rep.* 1997:10.

Yoshioka, S., Fransson, J. H. M. & Alfredsson, P. H. 2003 Evolution of disturbances in a boundary layer with wall suction. *Proc. Third Intl Symp. on Turbulence and Shear Flow Phenomena – 2003 TSFP-3, Sendai International Center, Sendai, Japan, 25–27 June* (to appear).